©2018

Syed R. Huq

ALL RIGHTS RESERVED

ION DYNAMICS OF ETHYLAMMONIUM NITRATE BY MEANS OF QUASIELASTIC NEUTRON SCATTERING

By

SYED R. HUQ

A thesis submitted to the

School of Graduate Studies

Rutgers, The State University of New Jersey

In partial fulfillment of the requirements

For the degree of

Master of Science

Graduate Program in Chemistry and Chemical Biology

Written under the direction of

Robert Hayes

And approved by

_____

_____

_____

_____

New Brunswick, New Jersey

October 2018

ABSTRACT OF THE THESIS
ION DYNAMICS OF ETHYLAMMONIUM NITRATE BY MEANS OF QUASIELASTIC

NEUTRON SCATTERING

By SYED R. HUQ

Thesis Advisor:

Robert Hayes

Ionic Liquids (ILs) are salts with a melting point below 100 ˚C. In recent years, ILs have garnered popular interest in academia and industry due to their unique properties and heterogeneous solvent nanostructure. In this Thesis, the solvent dynamics of one of the oldest, and most widely used ILs, ethylammonium nitrate (EAN) is examined using Quasi-Elastic Neutron Scattering (QENS) with H/D isotopic substitution. The data is fitted using analytical diffusions models and Bayesian statistics. The results show that long range cation motion in ILs is consistent with unrestricted (Fickian) translational diffusion. The measured cation diffusion coefficient of 3.96×10^{-11} m^2/s (298 K) is comparable to other self-assembled systems and two orders of magnitude slower than for molecular liquids (e.g. water @ 292 K, $D = 2.36 \times 10^{-9}$ m^2/s). The activation energy for all diffusion processes was independent of IL solvent within QENS instrument resolution and shown to follow Arrhenius dependence with temperature. These results demonstrate that long-range ion mobility in ILs is likely linked to revelations of long-range solvent nanostructure.

Acknowledgements

First and foremost I would like to express my gratitude and thanks to my advsior, Prof. Robert Hayes for dedicating his time to guide me in my research, providing the necessary foundation in my knowledge of chemistry to succeed, and lastly proofreading this thesis.

Next I would like to thank my committee members, Prof. Edward Castner Jr. and Laurence Romsted for their participation in my defense presentation and profound insight.

I owe my thanks to Andrew Nelson and Vanessa Peterson of the Australian Nuclear Science and Technology Organisation (ANSTO) for providing me with the data and opportunity to work on this project. I would also like to thank my group members, graduate students Krystal and Jonathan, and undergraduate students Natalie, Sara, and Mina for their positive influence and memories we shared over these two years.

Lastly, I want to show my sincere appreciation for my family for their constant support throughout my graduate studies.

Abbreviations

[EAN]	Ethylammonium nitrate
[PAN]	Propylammonium nitrate
AIL	Aprotic Ionic Liquid
BASIS	Backscattering silicon spectrometer
DSC	Differential scanning calorimetry
EISF	Elastic incoherent structure factor
FWHM	Full-width half maximum
FWS	Fixed window scan
HFBS	High-flux backscattering spectrometer
HWHM	Half-width half maximum
IL	Ionic Liquid
ND	Neutron diffraction
NIST	National Institute of Standards and Technology
NMR	Nuclear magnetic resonance
ORNL	Oak Ridge National Laboratory
PIL	Protic Ionic Liquid
QENS	Quasi-elastic Neutron Scattering

Table of Contents

Abstract ii
Acknowledgements iii
Abbreviations iv
List of Tables vii
List of Figures viii
Chapter 1: Introduction 1
1.1 Ionic Liquids 1
1.1.1 Definition 1
1.2 IL Structure and Dynamics 3
1.2.1 IL Structure 3
1.2.2 IL Dynamics 11
1.3 Neutron Scattering 20
1.3.1 Theory 20
1.3.2 Contrast Variation 21
1.3.3 Elastic, Inelastic, and QENS 22
1.3.4 Coherent vs. Incoherent 24
1.4 Liquid Dynamics 25
1.4.1 Fickian Diffusion 25
1.4.2 Jump Diffusion 27
Chapter 2: Materials and Methods 29
2.1 Materials 29
2.1.1 Synthesis and Characterization 29
2.1.2 Scattering Cross Sections for studied ILs 30
2.2 Neutron Instrument Details 30
Chapter 3: Data Analysis 33
3.1 Fitting Routine 33
3.1.1 Bayesian Theory 33
Chapter 4: Cation dynamics in ethylammonium nitrate (EAN) 36
4.1 Fixed Window Elastic Scan (FWES) 36
4.2 Low Temperature dynamics in [EAN] 39
4.2.1 Elastic Incoherent Structure Factor (EISF) 39
4.3 Liquid State Dynamics 43

4.3.1 Dynamic Structure Factor S(Q) 43
4.3.2 Line-width Analysis 47
Chapter 5: Conclusions and Outlook 51
Chapter 6: Bibliography 54
Chapter 7: Appendix 60
7.1 d_3-EAN data from HFBS 60
7.2 EAN data from BASIS 67
7.3 d_3-PAN Data from HFBS 71

List of Tables

Table 1. Representative cations and anions found in ionic liquids **3**
Table 2. Scattering Neutron Cross Sections of the Studied Species **30**
Table 3. HFBS Instrument Details **32**
Table 4. BASIS Instrument Details **32**

List of Figures

Figure 1. Schematic comparison between the structure of dilute electrolytes, concentrated electrolytes, and solvent-free, non-aqueous electrolytes which are composed only of ions. Solvent molecules are depicted as grey spheres, cations are yellow spheres and anions are green pentagons **2**

Figure 2. Walden plot of the log(molar conductivity, Λ) against log(reciprocal viscosity η^{-1}). The solid line is an ideal line for a complete dissociation of ions in a strong aqueous electrolyte (KCl_{aq}) **6**

Figure 3. (a) The proposed hydrogen-bonded structure of EAN in comparison to water's tetrahedral structure (b)..... **7**

Figure 4. A comprehensive comparison of neutron diffraction data. (Top) The neutron diffraction data that is fitted with EPSR for EAN and PAN. Deuterated contrasts are shown. Note the arrow pointing to the position of the bulk correlation peak. (Middle) Snapshot of the front face of fitted EAN and PAN bulk structure at thermal equilibrium (298 K). (Bottom) sdf plots of the anion central atom distribution as a function of distance and angle. The 20% probability surfaces are shown for the radial limits listed..... **9**

Figure 5. (a) Dielectric loss $\varepsilon''(\nu)$ spectra of neat EAN. Symbols represent experimental data and the lines are fits obtained from a dielectric relaxation model. (b) Rotational correlation times obtained from fs-IR (red) and DR spectroscopy (blue). The lines are fitted from an Arrhenius equation. Inset shows the ratio of correlation times (τ_{DR} / τ_{IR}) measured at three select temperatures. The ratio is constant at 1.4..... **12**

Figure 6. (a) Arrhenius plot of the α-relaxation time constant for DRS and OKE data in comparison to EAN viscosity. (b) Stokes-Einstein-Debye relationship plot of DRS and OKE data. **14**

Figure 7. A visual comparison of a 600 ps trajectory at 400K for (a) methane and (b) ammonium in the IL $[Pyrr_{1,4}][NTf_2]$. Both methane and ammonium have similar molecular volumes. For the case of methane, the trajectory is described by caged motions with a jump transition covering a large area. For the case of ammonium there is only a single jump event while a smaller overall diffusive trace. **15**

Figure 8. Fitted dynamic structure factor of C_8mimTFSI measured at Q = 1.7 $Å^{-1}$ and T = 300 K. The curves are a result of fitting. The delta function represents motions which are too slow and undetectable by instrument resolution. While the two Lorentzian are indicative of two dynamic processes occurring over different timescales. **17**

Figure 9. Arrhenius plot of the diffusion coefficients for EMIm-BF_4 and BMIm-BF_4. The heavier IL by molecular weight is shown to have overall slower dynamics. There is little disparity between the self-diffusion coefficients measured by different nuclei. **19**

Figure 10. Scattering cross section comparison between X-ray and neutrons. Note that X-ray cross section increases as a function of atomic number *Z*, while neutron cross section is isotope dependent. The cross section of D is much smaller than of H. **21**

Figure 11. Example of multiple contrast patterns in the protic ionic liquid EAN. **22**

Figure 12. Schematic of a QENS spectra extracted from one Q (length-scale) detector. A beam of thermal neutrons with energy ($E= \hbar k_0/2m$) travels toward the sample as an incident wave vector (k_0). After penetrating the sample, the neutrons bounce off as a final wave vector (k_f). Energy and momentum transfer can be measured by detectors positioned at angles corresponding length-scales within the molecule of interest. Neutrons gain or lose energy. When $\Delta E = 0$, there is a sharp elastic peak in the spectra, $\Delta E \neq 0$ shows quasi-elastic broadening. **23**

Figure 13. A representation of the different models that can be applied to QENS line broadenings (HWHM) as a function Q^2: Fickian (dashed-dotted line), Chudley-Elliott (solid line), Singwi-Sjölander (dotted line), and Hall-Ross (dashed line). Here, the diffusion coefficient was kept constant to show the disparities in the models.. ..... **27**

Figure 14. Structure of the studied protic ionic liquid EAN. **30**

Figure 15. A Probability Distribution Function (PDF) plot. The relationship between probability and Chi-squared is shown. The arrow indicates the most probable set of parameters which best fit the data. **33**

Figure 16. Temperature dependence of fixed window elastic scan (FWES) of d_3-EAN upon cooling and heating (1 $K.min^{-1}$) over all Q values. The change in intensity arises from EAN phase transitions, which leads to differences in total inelastic scattering and is consistent with a thermally-activated stochastic motion. Hysteresis in the two curves is likely a consequence of a super-cooling in the glassy phase (S2). Data was normalized against the lowest temperature value at T = 4 K. Arrows point to critical points in the transition curves. **36**

Figure 17. (a) DSC heating trace of EAN (1 K/min rate). The small bump at 231 K corresponds to a solid-solid phase transition, while the additional peak (T = 283 K) near the melting peak (T = 286 K) is believed to be another solid-solid transition. (b) Ion packing in the crystal structure of EAN. **38**

Figure 18. Snapshot of the temperature dependence of fixed window elastic scan (FWES) of d_3-EAN upon cooling and heating (1 $K \cdot min^{-1}$) over all Q values. Values are shown < 100 K to highlight the linear dependence of the Lamb-Mossbauer effect **39**

Figure 19. QENS spectra divided into its elastic and quasi-elastic components **40**

Figure 20. Q-dependence of Elastic Incoherent Structure Factor (EISF) over the liquid (left) and solid (right) phase. The dashed curve is predicted EISF based on eq 17 for a three-fold methyl group rotation. Temperatures were measured below and above the melting point of EAN (T_m = 285 K). In the liquid phase, there is sharp decrease in elastic intensity. Error bars represent one standard deviation. **41**

Figure 21. Schematic of a three-fold symmetry of CH_3 proton rotation about a single axis to model EISF data in EAN's solid phase. **42**

Figure 22. Raw unfitted Dynamic Structure Factor S(Q) of d_3-EAN at T = 200 K. The data is taken on the HFBS instrument from a Q range of 0.3085 $Å^{-1} < Q <$ 1.7124 $Å^{-1}$. An unexpected dip in the intensity of the spectra occurs at Q = 0.6830 $Å^{-1}$ and 0.9307 $Å^{-1}$, indicating a convolution of the first sharp diffraction peak measured in S(q). Inset shows the relative peak intensities. **44**

Figure 23. Raw unfitted Dynamic Structure Factor S(Q) of EAN at Q = 0.3085 $Å^{-1}$. The data is taken on the HFBS instrument from a T range of 200K < T < 333 K. There is temperature dependence of intensity and line broadness, typical of QENS structure factors. Inset shows the relative peak intensities **44**

Figure 24. Upper Panel: A representative example of the fitted dynamic structure factor S(Q) of EAN measured at T = 296 K and Q = 0.5314 $Å^{-1}$. (symbols). The data is described by a dynamic process associated with a Lorentzian component (solid blue) of which the total fitting line (solid red) is composed of. Fit was performed in accordance with eq 18, details are further discussed in the text. Inset: Probability density function (PDF) for the figure of merit χ^2 for a 1 Lorentzian versus 2 Lorentzian fit as determined through Bayesian analysis. This demonstrates that 1 Lorentzian is sufficient to describe data without penalizing goodness of fit. In the lower panel, positive (blue) and negative (red) residuals between the fit function and raw data are highlighted. **46**

Figure 25. Fit results of the temperature dependence for half-width half maximum $\Gamma_{1/2}$ as a function of *Q* at liquid phase temperatures (> 285 K). Dashed lines were fitted with eq 20 describing a Fickian model. Details of fitting can be found in the text..... **48**

Figure 26. Arrhenius Plot of the diffusion coefficient *D* (red symbols) describing long-range diffusion as a function of the inverse temperature. Symbols denote the values of *D* obtained for the three liquid phase temperatures (297, 314 and 333 K respectively). Dashed line represents a fit modeled by the Arrhenius equation in eq 21. Activation energy of the translational process is Ea = 23.4 ± 1 kJ/mol. **50**

Figure 27. Arrhenius Plot of the long-range translation diffusion of several liquid systems. The data presented in this Thesis is shown for comparison. Literature values depicted for C_2mimBr, TEA-TF, [BuPy][Tf_2N], [C_{12}Py][Tf_2N], 8CB, and SDS micelles **50**

Figure 28. Possible contrasts of EAN **52**

Chapter 1: Introduction

1.1 Ionic Liquids

1.1.1 Definition

Solvents are widely employed by scientists to facilitate chemical reactions.[1] Conventionally, most of these solvents are *molecular* in nature, for example water, alcohols, amides, alkanes, etc. However, solvents are not spectators in chemical reactions. There are many examples in literature where the choice of liquid is the key determinant of reaction outcomes, reducing waste, or enhancing economic feasibility.[2-4] In this spirit, the search for new solvents which can offer better chemistries is a strong motivator for fundamental research into liquids and condensed phases, as well as understanding the molecular factors that dictate solvent performance.

Ionic Liquids (ILs) are one such a class of solvents. Unlike traditional solvent media, ILs are pure liquid electrolytes composed entirely of anions and cations. Formally, ILs are defined as salts with melting points below 100 ˚C.[2] For the last decade, ILs have garnered popular interest[5, 6] in many fields from chemistry to physics and materials science to biology due to their unique properties and potential industry applications, including ionic conductivity, wide electrochemical windows, high thermal stability, low vapor pressure, and solubility.[7] A schematic representation of ILs is provided in Figure 1 below, with comparison to other electrolyte types.

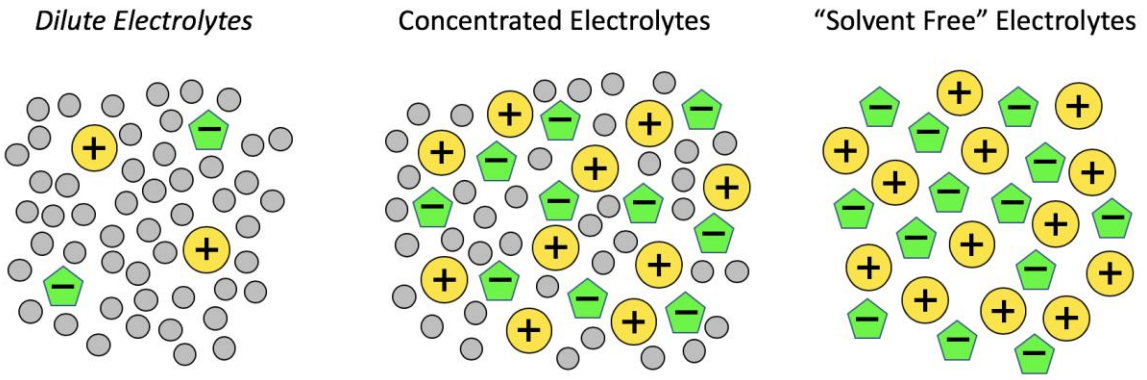

Figure 1. Schematic comparison between the structure of dilute electrolytes, concentrated electrolytes, and solvent-free, non-aqueous electrolytes which are composed only of ions. Solvent molecules are depicted as grey spheres, cations are yellow spheres and anions are green pentagons.

Ionic Liquids can be further subdivided into protic or aprotic.[8] Protic Ionic Liquids (PILs) are synthesized via an acid-base reaction through the transfer of a proton from a Brønsted acid to a Brønsted base.[9] This process is simple, economical, and without byproducts, although water can be difficult to remove. Cations include primary, secondary, or tertiary ammonium and imidazolium ions. Anions include organic, inorganic, or fluorinated compounds. In an ideal case, complete proton transfer in PILs leans to pure ionic media. However, there is a chemical equilibrium between product and reactants, meaning that the extent of proton transfer formation depends on the pK_a of the acid and base pair. In PILs, protons are available to undergo hydrogen bonding, a key feature which distinguishes PILs from Aprotic Ionic Liquids (AILs). AILs lack a unifying feature and can cover a wide variety of cation/anion chemical structures. Preparation of AILs is usually multi-step synthesis, the hallmark of which is the formation of new covalent bonds.

Some of the common IL cations and anions are shown below in Table 1.

Table 1. Representative cations and anions found in ionic liquids

Cations				
ammonium	pyrrolidinium	pyridinium	phosphonium	1-methyl-3-alkylimidazolium
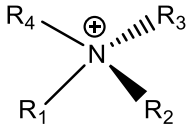	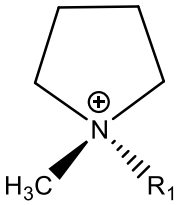	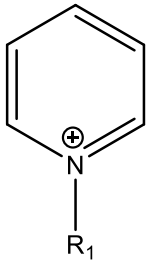	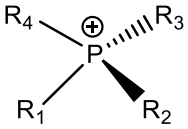	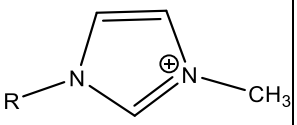
Anions				
halides	nitrates	sulfates	formate	hexafluorophosphate
	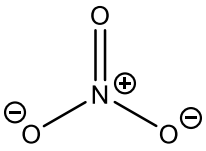	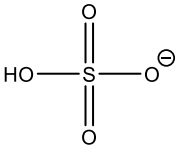	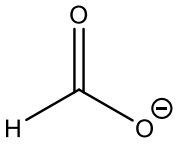	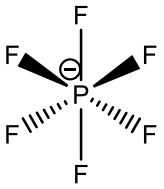

1.2 IL Structure and Dynamics

1.2.1 IL Structure

The bulk structure of ILs was previously thought to be reminiscent of classic models developed for molten salts and molecular liquids. In this ionic continuum, ions are diffusing rapidly and randomly through the bulk phase whilst maintaining local and long range electroneutrality, such that cations are solvated by a shell of anions and vice versa. For example, an early influential review by Dupont concluded "*1,3-dialkylimidazolium [ILs] possess analogous structural patterns in both the solid and liquid phase... although significant randomness in organization is necessary to describe the structure of a liquid.*"[10] It was not suspected at the time that additional long range ordering reminiscent of

surfactant self-assembly could be present in ILs in addition to local structure patterns common to other liquid types. In the following section, current understanding of IL structure in terms of ion pairs, supramolecular structures, and nanostructure is discussed. This is not meant to be comprehensive and is largely restricted to EAN that is the focus of this Thesis. Readers interested in IL structure are directed to several detailed reviews.[7, 11-14] Because IL dynamics is intimately linked to the manner in which ions are organized in space, a discussion of IL bulk structure is necessary to understand the results in this Thesis.

Some of the earliest models of IL structure stemmed from studies of molten salts and crystal lattices. At temperatures below their melting point, ILs exhibit nanoscale ion ordering consistent with local polar/apolar domain segregation of charged and uncharged groups. For example, bilayer crystal structures have been reported in common IL types such as for alkyl imidazolium[15-17] and alkyl pyridinium[18] cations. This organization is similar to the crystal structures of ionic amphiphiles.[19] Because cationic alkyl chains can adopt cis/trans conformations,[20] multiple crystal phases are possible. Such organization suggests similar patterns of self-assembly may be present upon melting.

Ion pairs are an obvious and important model for bulk structure of ILs and are a source of historical and recent interest for ion association in liquid phases.[21-24] In aqueous electrolytes, ion pairs are present and believed to represent the simplest structure unit.[25] For ILs specifically, this unit also merits discussion given that ILs evaporate as ion pairs.[26-28] It is thought that there are ion pairs along with free ions in the bulk solution. Conductivity measurements of EAN/octanol mixtures have suggested that for ethylammonium nitrate [EAN] the liquid phase is a chemical equilibrium between ion pair and free ions ($[EA^+][NO_3^-] \rightleftarrows EA^+ + NO_3^-$);[29] with ion pairs favored in pure bulk phase.

Dielectric spectroscopy and NMR suggest that ion pair formation is lacking for many of a wide range of aprotic[30] and protic ILs.[31] These techniques span across fast (pico-nano) and slow (micro-milli) second time scales,[32] which will be addressed in subsequent sections. In both cases, no evidence of ion pair formation is detected in the spectra. This suggests that ion pairs, if present, must exist on exceptionally long timescales[13] or are rapidly and constantly dissociating into free ions.[33, 34]

Macroscopic properties like conductivity or vapor pressure are dependent on the speciation of ions in the bulk; the movement of net neutral unit ion pairs should be slavish compared to univalent "free ions" in conductivity measurements. This would lead to departures from ideality and lower than expected conductivity values versus fluid viscosity. However, in most ILs, this is not the case, as Walden plots of molar conductivity against fluidity show ideal or near-ideal behavior,[35] c.f. Figure 2. For all these reasons, ion pairs are likely not sensible in models of IL structure and dynamics, and more relevant to other condensed phases.

Hydrogen bonding is a feature that is exhibited by many different ILs, and liquids generally. In 1981, it was first suggested that EAN may form a 3-D hydrogen bond network structure (Figure 3) similar to water due to proton donor and acceptor sites on the ions.[36] Evidence that EAN supported amphiphile self-assembly in the bulk phase was consistent with this, and the phase behavior and microstructure of the amphiphiles mimicked those in water.[36] More recently, far-IR measurements confirmed the presence of H-bonds in EAN and PAN via characteristic stretching, bending, and vibrational modes of N-H···O-H bonds at low wavenumbers.[37] Complementary density functional theory (DFT) calculations quanitified the strength of H-bonding in PILs is ~49 kJ/mol (trimethylammonium

nitrate).[38, 39] Hydrogen bonding in ILs probably form between ions and stabilize their conformations.

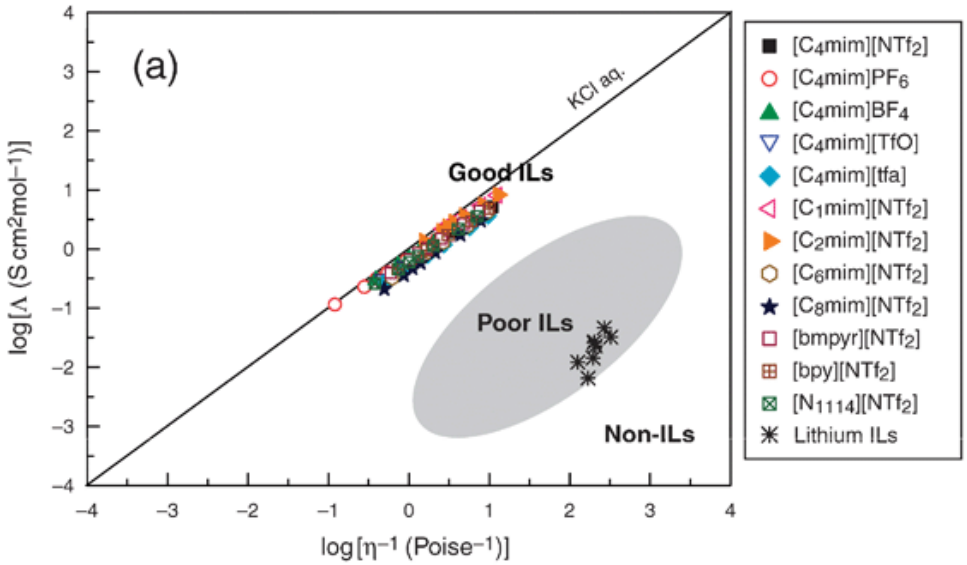

Figure 2. Walden plot of the log(molar conductivity, Λ) against log(reciprocal viscosity η^{-1}). The solid line is an ideal line for a complete dissociation of ions in a strong aqueous electrolyte (KCl_{aq}). Figure adapted from.[35]

Another model for IL bulk structure is ion clusters or aggregates, supported by the idea that ILs form supramolecular clustered structures to support the 3D H-bond networks.[10, 40] There are no formal specifications to define a "cluster" however.[32] Usually the cluster is defined as polydisperse aggregates of ions, reflected in the results of many mass spectroscopy studies.[41-47] Further spectroscopic measurements show that fluctuating hydrogen-bonded aggregates exist in the bulk with varying conformations.[17, 48-53] These ion interactions in a cluster are much more complex than a simple ion pair association in the form $[C_nA_{n-1}]^+$ for cation C and anions A, where n is typically > 5.

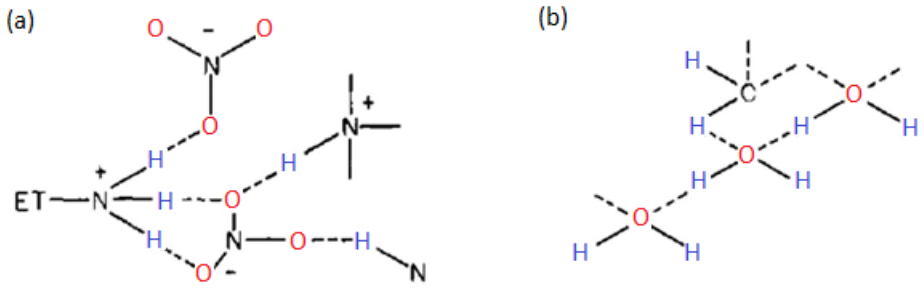

Figure 3. (a) The proposed hydrogen-bonded structure of EAN in comparison to water's tetrahedral structure (b). Hydrogen bonds are depicted as dashed lines. Figure was adapted from.[36]

Perhaps the most important development in this field is the concept of IL nanostructure, inviting comparison to other self-assembled phases. This long range solvent ordering, first predicted from computer simulations[54-56] and conductivity measurements,[57] was later confirmed in seminal work by Triolo et al. in X-ray diffraction (XRD) measurements.[58] At low scattering angles, a reasonably well-defined pre-peak or first sharp diffraction peak is detected for ILs that are sufficiently amphiphilic. A micelle-like model was used to explain this data, consistent with linear correlation between peak position and cation alkyl chain length; a 2.1 Å increase was observed for each additional CH_2 group.[58]

There are many external variables which may influence IL nanostructure. In general, most ILs[33, 59] and liquids[60] become more disordered as a function of temperature. In neutron diffraction studies for EAN and PAN, there were negligible differences in the spectra as a function of temperature, suggesting an invariant nanostructure.[61] Small- and wide-angle X-ray scattering (SAXS / WAXS) experiments by Greaves et al. showed that there was no change in the position of peak 1 as they were heated from 25 to 50˚C, however peak 2 had a slight decrease in *q*, which correlates to a ~1 Å increase in bulk correlation between alkyl

chains.[62] For imidazolium or pyrrolidinium-based ILs, structural integrity is decreased when heating from the glassy phase to liquid phase.[60] Here, diffraction peaks become broader, and shifts to smaller length scales, indicating weakened long-range order in the bulk phase.[63] Notably, exceptions to this behavior have been reported in ILs. For example, $[P_{14,6,6,6}][NTf_2]$ was shown to have a sharper bulk correlation peak as temperature was increased.[64] Subsequent fits to the diffraction spectra revealed that in this liquid, the polar domains became more organized at higher temperature to offset the disorder in the apolar domains.

More recently, the bulk structures of the PILs EAN and PAN were determined using neutron diffraction in conjunction with empirical potential structure refinement (EPSR) modelling[61, 65, 66] shown in Figure 4.

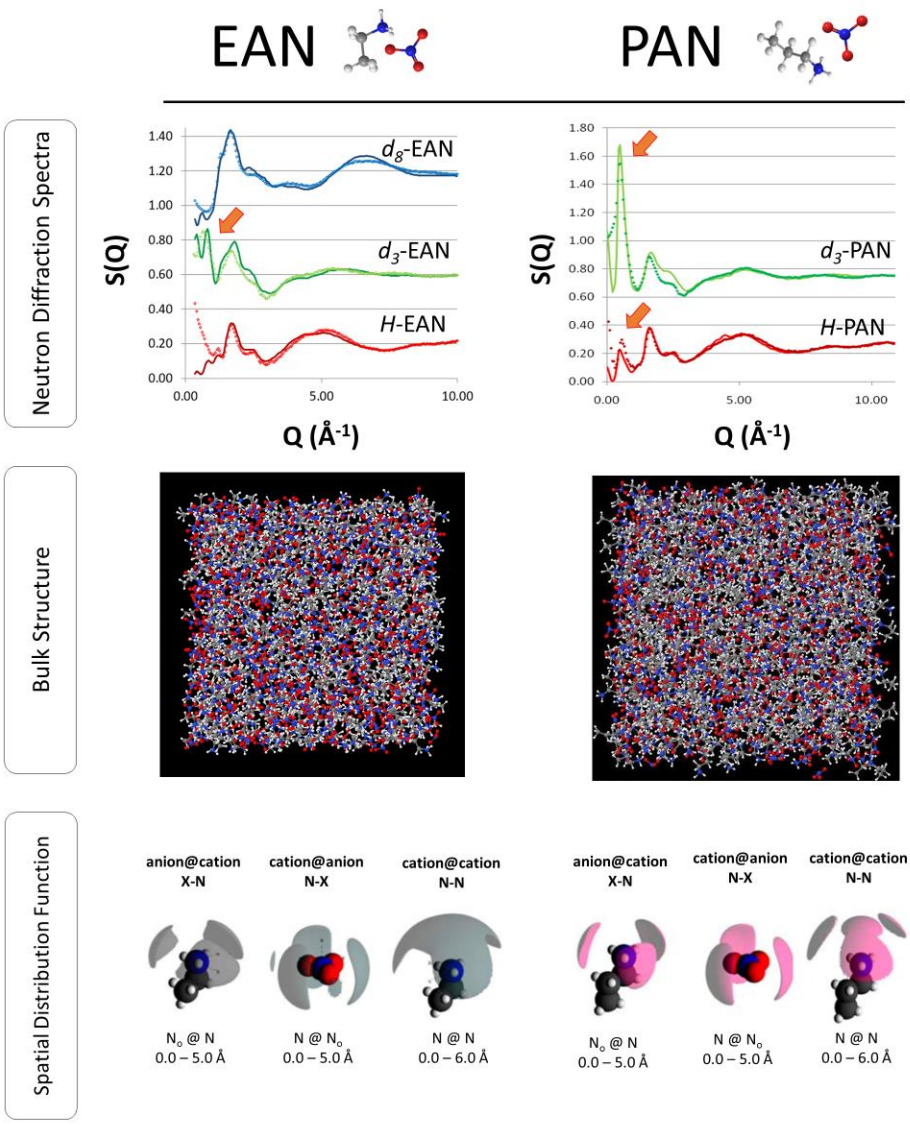

Figure 4. A comprehensive comparison of neutron diffraction data. (Top) The neutron diffraction data that is fitted with EPSR for EAN[61] and PAN[66]. Deuterated contrasts are shown. Note the arrow pointing to the position of the bulk correlation peak. (Middle) Snapshot of the front face of fitted EAN and PAN bulk structure at thermal equilibrium (298 K). (Bottom) sdf plots of the anion central atom distribution as a function of distance and angle. The 20% probability surfaces are shown for the radial limits listed.[65]

The diffraction pre-peak at low scattering angles highlighted with orange arrows indicate a bulk correlation length is present in both liquids of 10.1 Å for EAN[61] and 11.9 Å PAN.[66] Similar peaks were measured via SAXS/WAXS experiments by Greaves et al.[62] This unequivocally demonstrates a repeat bulk (nano)structure larger than the size of individual ions, and consistent with twice the dimension of an ion pair. Empirical Potential Structure Refinement (EPSR) modelling of the diffraction data reveal the origin of the pre-peak that arises because ionic molecular groups are segregated from alkyl chains, creating scattering contrast between ions of the same charge.[67] Similar conclusions have been drawn by many groups,[63, 68-71] notably by Castner and Margulis[64] from deconvolution of X-ray scattering spectra. For EAN and PAN, the results showed these liquids formed an L_3-sponge phase. This is reminiscent of surfactant self-assembly but on nanoscale dimensions and confirms that they are structurally heterogenous fluids.[72] At smaller length scales, spatial distribution functions (sdf) further provide evidence of local segregation of charged and uncharged groups. This is supported by bent hydrogen bonds in the charged domains.[73] Due to PAN having a longer alkyl chain length, the nanostructure is more pronounced with larger nonpolar domains. Furthermore, spatial distribution function (sdf) plots in Figure 4 also suggest that the alkyl chains in PAN are packed in an interdigitated manner. Subsequent work by the same group revealed that the reason the ILs adopt low-curvature sponge-like morphologies is that the preferred areas of the nonpolar and polar fragments in the nanostructure are similar.[65]

For EAN and PAN, the combination of neutron diffraction and EPSR yields the thermodynamically most stable structure that is consistent with the diffraction data.[61, 66] However, these results do not shed light on ion dynamics, and are time averaged snapshots

of ion self-assembly. Thus, open to question is cation and anion dynamics in this nanostructure, and how this compares to other solvent or self-assembled systems. In this Thesis, we seek to understand the dynamics of ions within the nanostructure using neutron scattering. Some of the key questions we addressed are:

- How do IL ions move within a pre-existing IL nanostructure?
- Are there differences for motions of charged vs. uncharged groups or anions vs. cations in the bulk?
- Is EAN dynamically heterogeneous in addition to structurally heterogeneous?

1.2.2 IL Dynamics

There have been many investigations of IL dynamics at both the molecular and macroscopic levels. MD simulations of aprotic ILs, sometimes verified against scattering data, indicated dynamic heterogeneity in the bulk phase that is correlated with structural heterogeneity.[74-79] Femtosecond optical-heterodyne-detected Raman-induced Kerr effect spectroscopy (OHD-RIKES) experiments were suggestive of dynamic heterogeneity in the bulk.[80] Other evidence of mesoscopic structure formed via aggregates originating from α-relaxations were measured using optical Kerr effect (OKE) spectroscopy and dielectric relaxation spectroscopy (DRS).[81]

The local structural reorganization of ILs around a solute and their ability to dissipate excess heat and energy provides information on ion dynamics.[82] Femtosecond IR spectroscopy was used to study heat dissipation in alkylammonium-based ILs[83] from vibrational signatures of N-D or N-H stretching modes. Hydrophobic domains equilibrate at a faster rate and have weaker interactions than corresponding charged domains. The

dynamics in the ionic domains were found to be virtually unaffected by the alkyl chain length, implying dynamic heterogeneity.[83]

In water, hydrogen bonds promote the presence of directional interionic interactions that causes molecular reorientation to occur via jumps instead of a diffusive mechanism.[84, 85] Dielectric relaxation spectroscopy and femtosecond-infrared spectroscopy (fs-IR) were used on ethylammonium nitrate (EAN) to show that the rotation of the EA cation takes place via large angular jumps of 106° (Figure 5).[86]

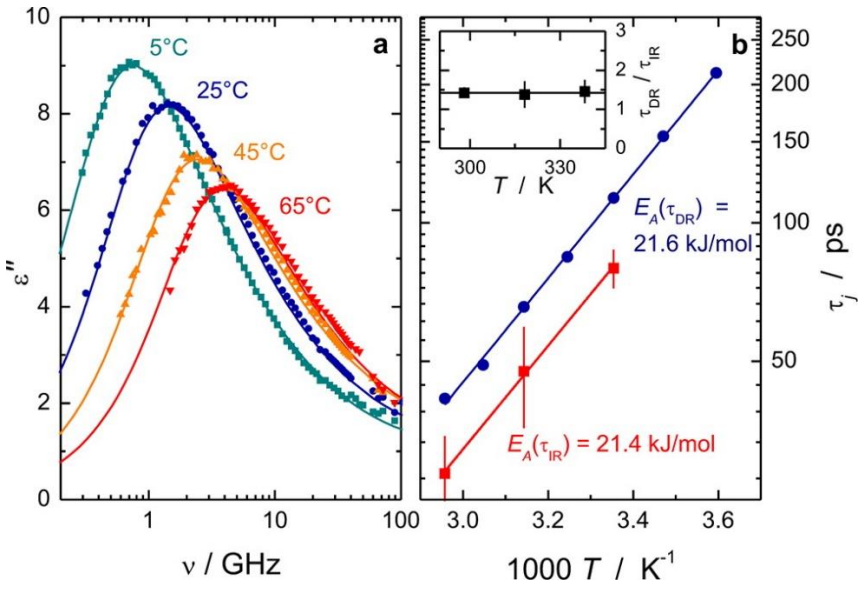

Figure 5. (a) Dielectric loss $\varepsilon''(\nu)$ spectra of neat EAN. Symbols represent experimental data and the lines are fits obtained from a dielectric relaxation model. (b) Rotational correlation times obtained from fs-IR (red) and DR spectroscopy (blue). The lines are fitted from an Arrhenius equation. Inset shows the ratio of correlation times (τ_{DR} / τ_{IR}) measured at three select temperatures. The ratio is constant at 1.4, Figure adapted from.[86]

In dielectric relaxation spectroscopy (DRS), electrical polarization was measured as a function of field frequency for EAN. In Figure 5a, rotational relaxation of the $C_2H_5NH_3^+$ cation has a characteristic maximum ν_{max} that shifts to higher frequencies as a function of temperature. This suggests faster rotational dynamics with temperature and is consistent with Arrhenius behavior with activation energy $E_A(\tau_{DR})$ = 21.6 kJ mol^{-1}. Similar behavior was seen in fs-IR experiments[86], with activation energy of $E_A(\tau_{IR})$ = 21.4 kJ mol^{-1} (Figure 5a).

More recent DRS and OKE studies by Turton et al. probed the terahertz dynamics and slow relaxations of EAN.[31] There are two overall processes observed, librations and an α-relaxation. The α-relaxation is associated to molecular reorientations and is detected via both experimental methods and shown to follow Arrhenius temperature dependence. This paper showed decoupling between viscosity and diffusivity, effectively violating the Stokes-Einstein-Debye (SED) relation (Figure 6) and fitted to the Vogel-Fulcher-Tammann equation:[87, 88]

$$D = D_0 \exp\{B/(T - T_0)\} \quad (1)$$

Where T_0 is the ideal glass-transition temperature that is usually 30-60 K below the calorimetric glass transition temperature T_g for both ionic and molecular liquids.[89]

This departure of SED model strongly implies enhanced solvent structure in the bulk consistent with L_3-sponge-like morphologies detailed in the last section.

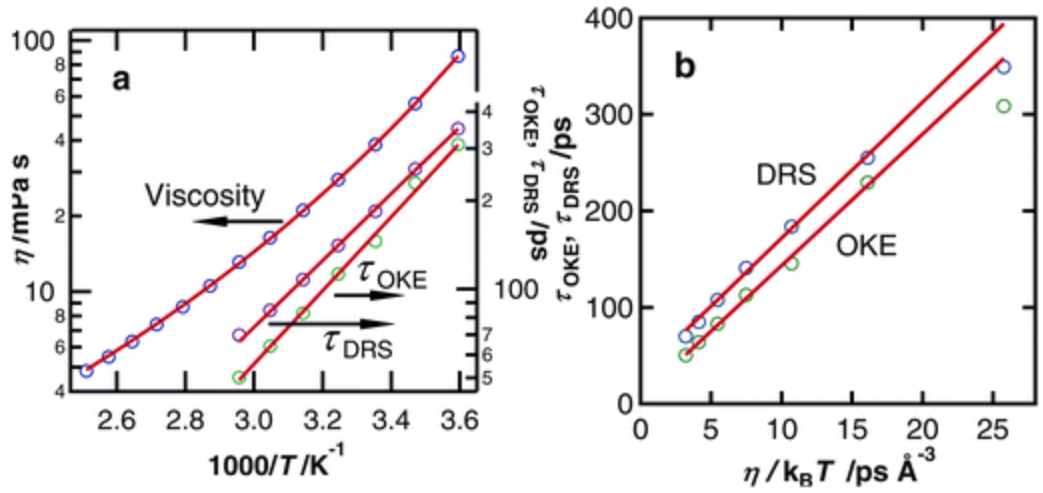

Figure 6. (a) Arrhenius plot of the α-relaxation time constant for DRS and OKE data in comparison to EAN viscosity. (b) Stokes-Einstein-Debye relationship plot of DRS and OKE data.

A fascinating study by Margulis et al. shows how small solutes diffuse based on their charge and preference for polar and apolar domains, c.f. Figure 7.[67] Based on the Stokes-Einstein prediction, one would expect that the diffusivity of the two probe molecules, methane and ammonia, to be comparable due to having similar radius and tetrahedral geometry. However, the MD simulations showed that neutral methane solute simply acts as a spectator which participates in fast jumps across the soft, mobile apolar regions. On the other hand, the ionic ammonia solute becomes integrated as part of the IL charged domains and there is dynamic coupling driven by charge-charge interactions. Therefore, the motion of small, charged solutes is typically slow on the same timescale. This study provides insight on the mechanism of transport for ILs, showing both size and charge dependence, and provides clues for how the IL ions themselves behave.

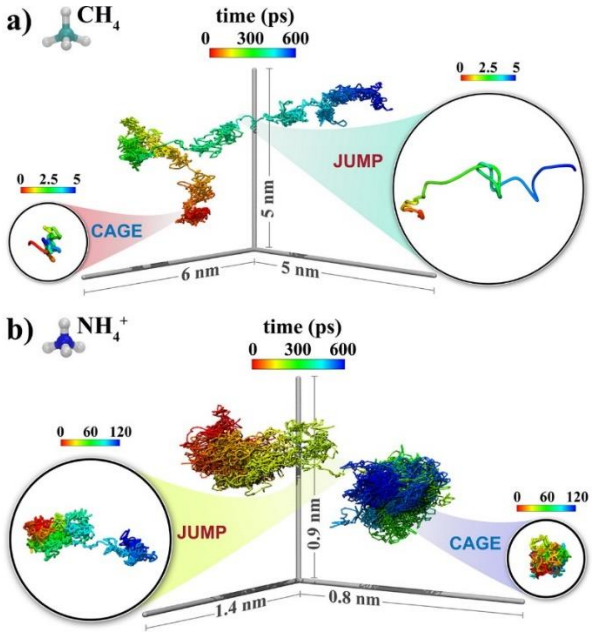

Figure 7. A visual comparison of a 600 ps trajectory at 400K for (a) methane and (b) ammonium in the IL $[Pyrr_{1,4}][NTf_2]$. Both methane and ammonium have similar molecular volumes. For the case of methane, the trajectory is described by caged motions with a jump transition covering a large area. For the case of ammonium there is only a single jump event while a smaller overall diffusive trace.

Quasi-elastic Neutron Scattering (QENS) is an important experimental technique to examine liquid dynamics on a hierarchy of length and time scales and is sensitive to changes in temperature *T*. This enables powerful examination of the nature of the IL dynamics, and how it is linked to structure. QENS can obtain characteristics of observed dynamics such as radii of confinement, diffusion coefficient, and jump distances since neutron wavelengths correspond to interatomic distances in condensed matter.[90] Some researchers have recently applied this technique to the study of ILs, mainly the aprotic variety.[91-100] QENS however is limited, in most cases, because only cation dynamics are

detected due to the large incoherent scattering cross section of hydrogen atoms that are a hallmark of cation alkyl chains. H/D isotopic labelling enables different motions of the IL cation to be highlighted, relating to dynamics in the polar and apolar regions of the liquid.[97, 98] The dynamic structure factor obtained S(q, ω) via QENS can be fitted and the number of dynamic processes can be quantified. A common theme of QENS studies of ILs possessing alkyl chains is that at low temperatures, thermally activated methyl groups rotations occur at very low temperatures (T < 100 K),[91, 98] followed by long-range diffusion in Fickian or jump-diffusion models. Interestingly, these models assume a strong degree of liquid structure between ions and where diffusion occurs in successive discrete jumps. For example, Burankova et al. showed that the dynamics of the IL C_8mimTFSI is described by two localized processes occurring on the picosecond time scale[101] c.f. Figure 8. The two relaxation processes have energy transfer ranges in the ±1 meV and ±2 meV regimes, which suggests both “fast” and “slow” cation motions are present (respectively).

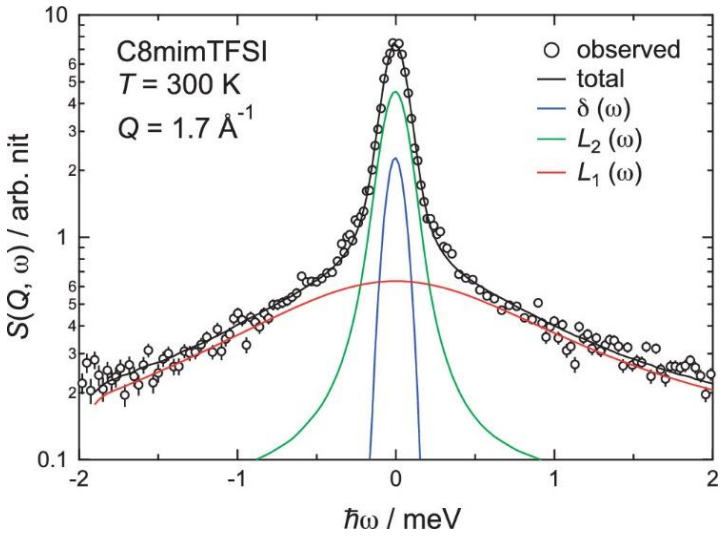

Figure 8. Fitted dynamic structure factor of C_8mimTFSI measured at Q = 1.7 $Å^{-1}$ and T = 300 K. The curves are a result of fitting. The delta function represents motions which are too slow and undetectable by instrument resolution. While the two Lorentzian are indicative of two dynamic processes occurring over different timescales.

Other published work by Burankova et al. made use of QENS and H/D labeling to compare cation diffusion in aprotic and protic ILs.[95-99] Overall, it was found that for each IL above the melting transition, elastic contribution disappears and instead there is quasi-elastic broadening in the dynamic structure factor S(q, ω). Data for these ILs were well fitted by Lorentzian and Gaussian functions to describe each dynamic process. Thermally activated methyl group rotations were the first dynamic process to be detected.[99] Some differences in localized motions were also characterized (e.g. NH_3 rotations), but all share slow long-range diffusion in the liquid phase. This type of motion describes the unrestricted, translational diffusion of cations. Values for long-range diffusion vary over several orders of magnitude ($\times 10^{-11}$ m^2/s to $\times 10^{-8}$ m^2/s).[96-98, 100-102]

QENS on N,N,N′,N′-tetramethylguanidinium bis(perfluoroethylsulfonyl)imide, a protic ionic liquid, yielded four distinct dynamic processes across solid and liquid phase.[100] At low temperatures, localized side group rotations of $-CH_3$ and $-NH_2$ groups are seen on the nanosecond timescale due to their relatively low energy barrier. When the PIL melts, there are two new diffusional processes of translational character occurring. Of these two processes, they are further classified into unrestricted/restricted diffusion. The former is associated to long-range proton transfer while the latter is a faster, spatially restricted motion that occurs for the cation within a confinement radius of 8 Å, consistent with the likely nanostructure in this IL. These studies show evidence of the onset of diffusional processes within PIL phase transitions.

Nuclear Magnetic Resonance (NMR) spectroscopy studies provide an expansive range of tools which can be used to probe IL structure and dynamics.[32] The relaxation times obtained correspond to the rotational dynamics of ions. NMR spectroscopy can be applied to either anion or cation dynamics as many different nuclei can be tracked. Most common ILs offer nuclei which have spin-½ or quadrupolar spin >½ such as ^{1}H, ^{13}C, ^{15}N, ^{19}F, ^{2}H, ^{11}B, ^{14}N, or ^{35}Cl. Typically ^{1}H and ^{19}F are used for experiments due to high abundance and large gyromagnetic ratio, although experiments using ^{7}Li, ^{11}B, and ^{13}C have been documented.[103, 104]

Pulse-field gradient spin-echo (PFGSE) NMR yields information on self-diffusion coefficients of ILs over broad temperature ranges. Ionic diffusion and other transport properties such as viscosity can be classified as Arrhenius or non-Arrhenius in accordance to their temperature dependence. For liquids, viscosity is inversely proportional to temperature, while diffusion is directly proportional. In the case that it deviates from

Arrhenius behavior, it can be described by the Vogel-Fulcher-Tammann (VFT) equation.[105]

Cation and anion dynamics can be tracked simultaneously. For example, the ionic self-diffusion coefficients of ^{19}F and ^{11}B nuclei can be used to detect BF_4^- anions, while ^1H nuclei for the C_2mim^+ cations (Figure 9). This shows a bifurcation in IL dynamics that depends on whether the ion is positively or negatively charged.[106] Together, these results suggest that in addition to dynamic heterogeneity among the charged and uncharged regions in EAN, the EA^+ cations may be moving at a different rate to the NO_3^- anions.

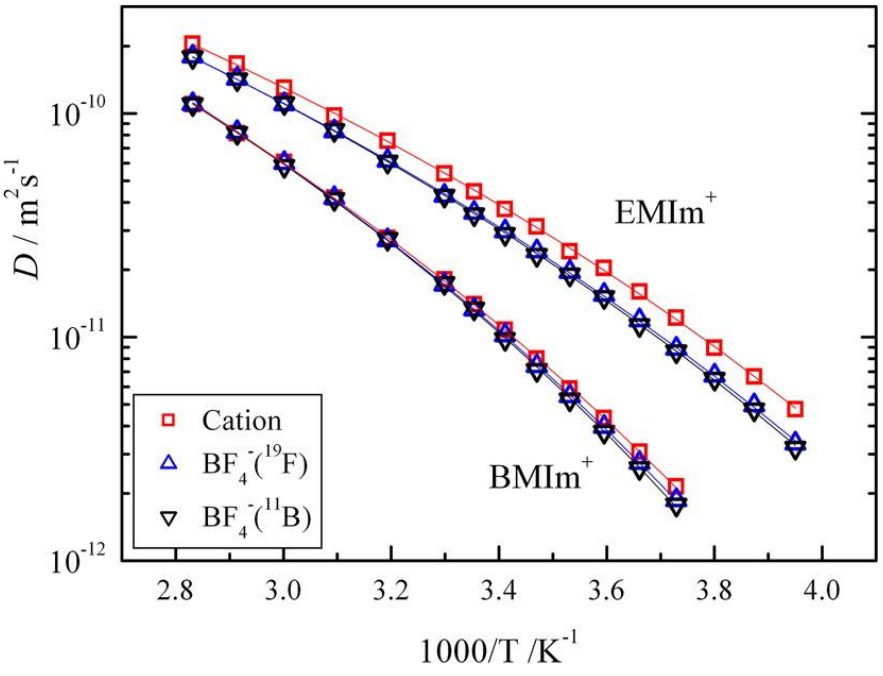

Figure 9. Arrhenius plot of the diffusion coefficients for EMIm-BF_4 and BMIm-BF_4. The heavier IL by molecular weight is shown to have overall slower dynamics. There is little disparity between the self-diffusion coefficients measured by different nuclei. Figure is adapted from.[106]

1.3 Neutron Scattering

1.3.1 Theory

The 1994 Nobel Prize in Physics citation for Brockhouse and Shull (1994) stated *"Neutrons tell you where the atoms are and what the atoms do."*[107] Since the development of the technique in 1945, neutron scattering has emerged as a powerful and versatile experimental tool to study structure and dynamics at atomic and molecular length and timescales, for scientists in many disciplines.[108-114]

Neutrons are neutral subatomic particles with a mass of m = 1.0087 amu, spin = ½ and magnetic moment of μ_n = -1.9132 nuclear magnetons.[109] The concept of matter as waves was first proposed by de Broglie in 1924, [115] and subsequently awarded a Nobel Prize for in 1929. This relationship is described by the following equation:

$$\lambda = \frac{h}{p} \tag{2}$$

where the wavelength λ of a particle is related to its mass p through Planck's constant h.

Neutrons possess many properties which make them ideal for probing condensed matter. Firstly, as a neutral species they are deeply penetrating. Second, the wavelength of neutrons is comparable to interatomic spacings, enabling diffraction patterns. Third, the energies of cold neutrons are comparable to that of molecular motions in solid and liquids samples.

Unlike X-rays, which interact with the electron cloud, neutrons interact with the nuclei. The scattering length b, and subsequently scattering cross section $\frac{d\sigma}{d\Omega}$ defines the likelihood of interaction differs for different atoms. While the scattering cross section increases as a function of atomic number Z for X-Rays, there is no simple trend for neutrons (Figure 10).

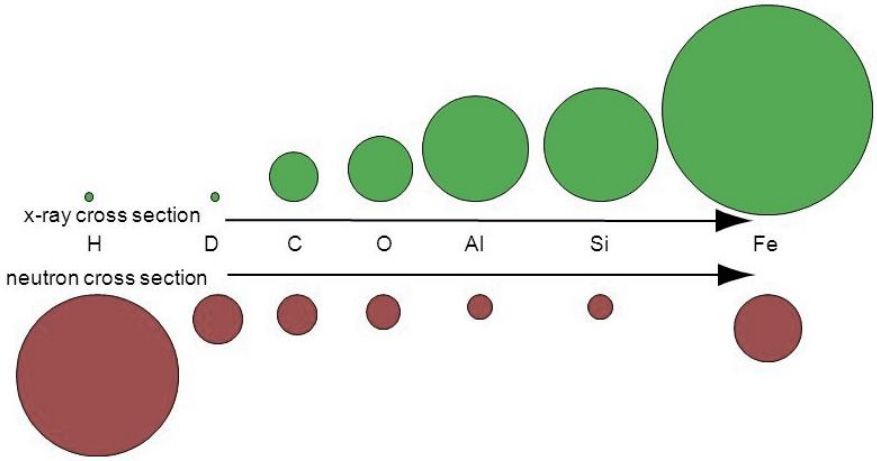

Figure 10. Scattering cross section comparison between X-ray and neutrons. Note that X-ray cross section increases as a function of atomic number *Z*, while neutron cross section is isotope dependent. The cross section of D is much smaller than of H.

1.3.2 Contrast Variation

Isotope substitution is a powerful approach to elucidating the structure of the condensed phase, particularly in soft matter. The scattering lengths of hydrogen (^{1}H) and deuterium (^{2}H) are opposite in sign, and hydrogen has a much larger cross section. Hence, selective deuteration can give rise to multiple diffraction spectra of the same compound (Figure 11).

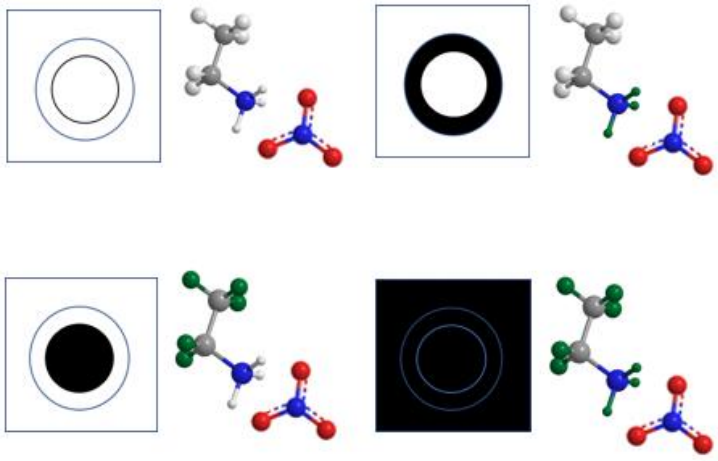

Figure 11. Example of multiple contrast patterns in the protic ionic liquid EAN.

This is not possible in X-ray scattering, and thus neutrons are ideal for probing hydrogen-rich materials. Condensed matter systems are ordered on the angstroms to nanometer length-scale and possess dynamics within the electron-volt (eV) energy range. X-ray wavelengths for the most part is in the range of a few angstroms, but their corresponding energies are too large and reside in the kilo electron-volt (keV) range. Similarly, in Raman (IR) or Brillouin (light) scattering, wavelengths are too large for diffraction.

1.3.3 Elastic, Inelastic, and QENS

The geometry of a neutron scattering event is shown in Figure 12. A pulsed beam of thermal neutrons with energy ($E= \hbar k_0/2m$) and wavelength λ travel toward the sample as an incident wave vector (k_0). After penetrating the sample, the neutrons diffract as a final wave vector (k_f). Energy and momentum transfer can be measured by detectors positioned at angles corresponding to length-scales within the molecule of interest.

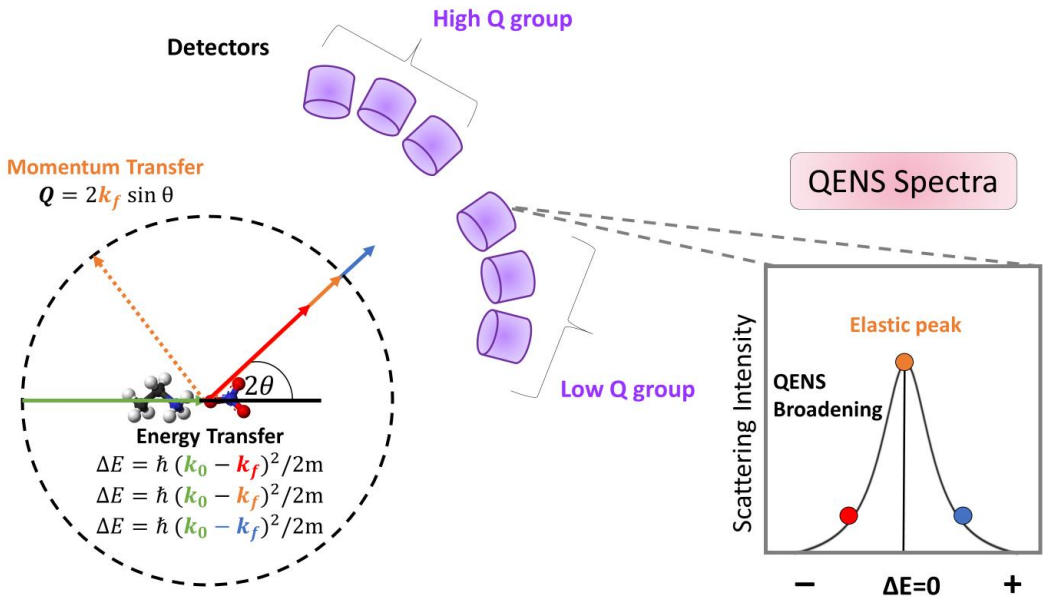

Figure 12. Schematic of a QENS spectra extracted from one Q (length-scale) detector. A beam of thermal neutrons with energy ($E = \hbar k_0/2m$) travels toward the sample as an incident wave vector (k_0). After penetrating the sample, the neutrons bounce off as a final wave vector (k_f). Energy and momentum transfer can be measured by detectors positioned at angles corresponding length-scales within the molecule of interest. Neutrons gain or lose energy. When $\Delta E = 0$, there is a sharp elastic peak in the spectra, $\Delta E \neq 0$ shows quasi-elastic broadening.

Diffracted neutrons of high and low scattering angles are detected. As the collision between neutrons and sample may result in a loss or gain in energy, it is classified as elastic or inelastic scattering.[108-111, 114, 116] Elastic scattering occurs when there is no change in energy $\Delta E = 0$. Here, the pre- and post-collision kinetic energy of the neutrons are equal. On the other hand, neutron interactions with matter may result in discrete losses or gains of energy $\Delta E \neq 0$, and so the final energy of the neutrons may be net *positive* or *negative* in inelastic scattering. Many molecular level processes can induce inelastic scattering, such as band vibrations and stretching modes.

A third, hybrid category of neutron scattering known as Quasi-elastic Neutron Scattering (QENS)[90] involves small energy exchanges of neutrons in a scattering event. This leads to an energy broadening around the elastic peak and is attributed to molecular level processes in the sample that occur with a distribution of energies rather than a step-wise regiment. Molecular rotations are examples of such processes,[90] thus QENS is an ideal method to probe liquid dynamics at the molecular level with H/D substitution.

A restriction in QENS technique relates to the instrument. There are many different types of QENS spectrometers - time-of-flight, backscattering, etc. The differences in these spectrometers is the way the neutrons scatter from the beam onto the sample and their respective energy resolution. For example, in this Thesis, data from two backscattering spectrometers, HFBS at Oakridge National Laboratory (ORNL) and BASIS at National Institute of Science and Technology (NIST) differ. The core strength of QENS experiments is that atomic and molecular diffusion in short-range motions such as rotations can be quantitatively determined at high resolution. We have deliberately used two instruments to compare the dynamics probed at different resolutions.

1.3.4 Coherent vs. Incoherent

The double differential cross section $\frac{d^2\sigma}{d\Omega d\omega}$ is an important quantity in a scattering experiment that is attributed to the number of neutrons scattered per second into a solid angle with a final energy. This quantity contains both a coherent and incoherent contributions:

$$\frac{d^2\sigma}{d\Omega d\omega} = \left(\frac{d^2\sigma}{d\Omega d\omega}\right)_{coh} + \left(\frac{d^2\sigma}{d\Omega d\omega}\right)_{inc} \quad (3)$$

When particles have the same scattering length *b*, this leads to coherent scattering. This is dependent on momentum transfer *Q* which contains information on structure. Correlations between the nuclei allow coherent scattering to describe collective dynamics of nuclei. Deviations from this behavior leads to incoherent scattering, which describe the dynamics of individual particles. Separating the coherent and incoherent scattering signals is difficult. Because most soft matter samples are hydrogen-rich, incoherent scattering dominates and thus the motions in condensed matter detected by QENS are primarily incoherent.[117]

1.4 Liquid Dynamics

1.4.1 Fickian Diffusion

The study of the diffusion of one solution into another was first performed by Thomas Graham in 1950.[118-120] Through several experiments, he distinguished colloids on behalf of their diffusion rates through membranes.[121] Subsequent work by Adolf Fick, defined the "Fick's Laws of diffusion" which frequently appear in literature.[122] Fick's Laws state that solutes diffuse from a region of high concentration to a region of lower concentration. Fick defined diffusion coefficients with his First law:

$$J = -D \bullet dc / dx \quad (4)$$

Where *J* is the one-dimensional flow pe nit area per unit time, *D* is the diffusion coefficient, and lastly *c* is the concentration per unit volume. The derived equation, or Fick's second law, is written as:

$$dc/dt = -\frac{d}{dx}\left(D\frac{dc}{dx}\right) \tag{5}$$

In the case of long-range self-diffusion i.e. small-Q incoherent neutron scattering is concerned, the self-correlation function obeys Fick's second law, and can be thus re-written as:

$$\frac{\partial}{\partial t}G_s(r,t) = D_s \nabla^2 G_s(r,t) \tag{6}$$

With the initial condition that $G_s(r, t=0) = \partial(r)$. This implies that diffusional processes are treated as if all diffusing particles start at the origin at time zero. The solution of the diffusion equation on long length scales is:

$$G_s(r,t) = (4\pi D_s |t|)^{-3/2} \exp\left(-\frac{r^2}{4D_s|t|}\right) \tag{7}$$

The spatial Fourier transformation of this yields the self-part of the intermediate scattering function that is first detected by the neutron instrument:

$$I_s(Q,t) = \exp(-Q^2 D_s t) \tag{8}$$

Another sequential Fourier transformation in time will finally yield the Incoherent scattering function:

$$S_{inc}(Q,\omega) = \frac{1}{\pi}\frac{\hbar D_s Q^2}{\left(\hbar D_s Q^2\right)^2 + \left(\hbar\omega\right)^2} \tag{9}$$

This scattering law is typically described by a Lorentzian function whose half-width half maximum (HWHM) is written as:

$$\Gamma = \hbar D_s Q^2 \tag{10}$$

At small Q, this is generally referred to as the Q^2 law and is valid for systems with linearly increased line broadness as a function of Q. When plotting QENS spectral line widths as a function of Q^2, if a straight line is obtained then Fick's Law is obeyed. Thus, Fickian diffusion involves unrestricted, long-range motion, devoid of any boundary conditions or restrictions.

1.4.2 Jump Diffusion

Fick's law is a simplified description of long-range translational diffusion. In many cases, diffusion is limited by several factors: confinement, strong interactions, bond restrictions, etc. In such cases diffusion may deviate from Fick's DQ^2 law, since overall motion of diffusion is now broken down into elementary steps, other models need be considered.[123] Examples of these models are summarized in Figure 13.

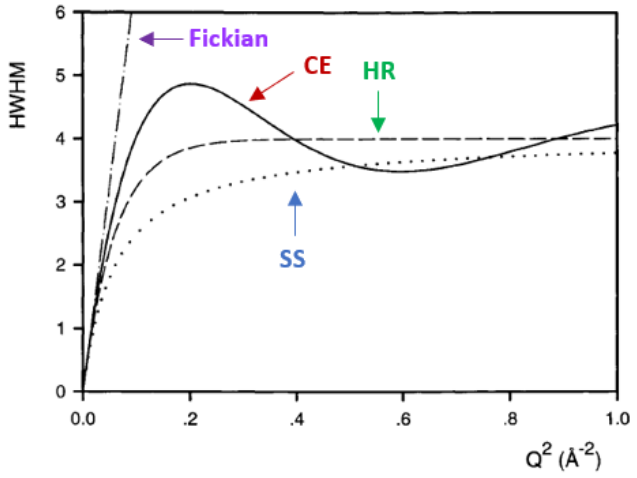

Figure 13. A representation of the different models that can be applied to QENS line broadenings (HWHM) as a function Q^2: Fickian (dashed-dotted line), Chudley-Elliott (solid line), Singwi-Sjölander (dotted line), and Hall-Ross (dashed line). Here, the diffusion coefficient was kept constant to show the disparities in the models. Adapted from.[124]

Jump diffusion models describe the characteristic (1) length and (2) time of such elementary steps. The general physical description is as follows: atoms caged by neighbors vibrate at a site for residence time τ, upon a vacancy at another site they jump for a distance *d*, with *n* jump possibilities.[124] The jump time is negligible relative to the residence time and disregarded. Irrespective of the overall details of any diffusion process, any long-range model converges to Fickian Law at small *Q*. At higher *Q*, corresponding length-scales become smaller and line-widths reach an asymptotic value of 1/τ.

The Chudley-Elliot (CE) model for liquid diffusion assumes local lattice-like structure.[125] Because of structural integrity, jump length *d* is assumed to be held constant. It has been reported previously to describe diffusion within highly-structured zeolites.[126] CE model is shown in the equation below:

$$\Gamma = \frac{1}{\tau}\left(1 - \frac{\sin(Qd)}{Qd}\right) \tag{11}$$

Next is the Singwi-Sjölander (SE) model which describes diffusion as a series of random jumps[127] instead of fixed hopping like in CE model. This model is commonly found in QENS literature, and has been shown to fit not only ILs[102] but other molecular liquids and glassy systems. SS model is written as:

$$\Gamma = \frac{\hbar DQ^2}{1 + DQ^2\tau} \tag{12}$$

Lastly, the Hall-Ross (HR) model assumes that the jump lengths in the system follow a Gaussian distribution, due to weak but random structure.[128] It is described as:

$$\Gamma = \frac{1}{\tau}\left[1 - \exp\left(-DQ^2\right)\right] \tag{13}$$

Chapter 2: Materials and Methods

2.1 Materials

2.1.1 Synthesis and Characterization

Two chemically identical, but isotopically different contrasts of EAN, were prepared for neutron scattering experiments: hydrogenous (*H*-) or partially deuterated (D_3-, D_4-).

Hydrogenous (*H*-) EAN was prepared by equimolar combination of a Brønsted acid and Brønsted base. This involved dropwise addition of nitric acid (Sigma-Aldrich, 69%) to a chilled solution (<10°C) of hydrogenous ethylamine (Aldrich, 70%), and distilled water. During acid addition, the mixture was continuously stirred to disperse heat generated.

Water was removed from the mixtures by rotor evaporation for several hours at 40-50 °C. The resultant concentrated salt solution (H_2O content ~2% v/v%) was then purged for at least six hours with filtered N_2 gas and then heated overnight in an oil bath at 110 °C under a N_2 atmosphere. This led to pure PIL samples, with water contents < 20 ppm by Karl Fischer titration.

The partially deuterated D_3- contrasts was prepared *in vitro* by selectively replacing hydrogen with deuterium on the exchangeable ammonium group protons. This was achieved by washing volumes of the corresponding *H*- sample several times in excess fresh deuterium oxide (D_2O, 99% Sigma Aldrich) where mol:mol ratio of D_2O:PIL in the mixture >3:1. Excess aqueous solvent was removed via rotor evaporation after each wash. Previous ^{1}H-NMR experiments reveal that, on average, 2.5 out of 3 amino hydrogens are replaced with deuterium per wash in D_2O. In these experiments, the d_3- contrast were washed at least three times in excess D_2O.

2.1.2 Scattering Cross Sections for studied ILs

The chemical structure of ethylammonium nitrate is presented in Figure 14.

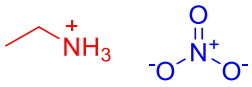

Figure 14. Structure of the studied protic ionic liquid EAN.

The scattering cross sections of the cation and anion are summarized in Table 2. The incoherent signal from the cation is much larger than the anion, and the observed dynamics is attributed to single-particle dynamics of the cation.

Table 2. Scattering Neutron Cross Sections* of the Studied Species

	species	σ_{scat} [b]	σ_{coh} [b]	σ_{inc} [b]	σ_{abs} [b]	$\sigma_{inc}/\sigma_{scat}$ [%]
Cations	$CH_3CH_2NH_3^+$	678.78	36.17	642.58	4.57	94.67
	$CH_3CH_2ND_3^+$	455.68	47.68	408.00	3.57	89.54
Anions	NO_3^-	24.21	23.71	0.50	1.90	2.07

*Values taken from [129]

2.2 Neutron Instrument Details

Neutron backscattering is a type of inelastic neutron scattering. Backscattering experiments are suited for studying atomic and molecular motions on the nanosecond time regime.

QENS measurements were performed on the BASIS instrument at the Spallation Neutron Source, ORNL (TN, USA) and HFBS instrument at the NIST Center for Neutron Research, (MD, USA). These two instruments were used because of their differences in energy windows which can probe into fast and slow dynamic processes. Initially, experiments were performed on the BASIS instrument whose energy window is wider. However,

subsequent experiments were repeated on the narrow-energy HFBS to focus solely on long-range translational motion.

Both instruments use Si(111) crystals to select an initial neutron energy.

For BASIS that corresponds to an energy of 2.08 meV (6.27 Å) for neutrons scattered by the sample. The dynamic energy and dynamic Q ranges are $-100 < \omega\ (\mu eV) < 100$ and $0.2 < Q\ (Å^{-1}) < 2.0\ Å^{-1}$ respectively.

For HFBS that corresponds to an energy of 2.08 meV (6.27 Å) for neutrons scattered by the sample. The dynamic energy and dynamic Q ranges are $-20 < \omega\ (\mu eV) < 20$ and $0.3085 < Q\ (Å^{-1}) < 1.712\ Å^{-1}$ respectively.

The IL samples were loaded in a sealed 0.1 mm thick annular Aluminium cylindrical cell to minimize noise and scattering inelastic effects. The temperature of the cell was controlled by a closed-cycle refrigerator to within ± 0.1 K.

The energy resolution of BASIS and HFBS averaged over all Q values is 3.5 and 1 μeV respectively. While the resolution function analysis was performed at 30 and 5 K for BASIS and HFBS.

Raw spectra were converted from time-of-flight to energy transfer spectra, using the standard corrections, normalizations and rebinning in Q, using standard HFBS data analysis software DAVE and MANTID. Covariance matrices were examined to make sure inter-parameter correlations were acceptable. All uncertainties are reported at the 1 standard deviation level.

Table 3. HFBS Instrument Details[130]:

Elastic energy	2.08 meV
Bandwidth	+/- 50 μeV
Elastic Resolution	1 μeV
Q range	0.25 - 1.75 $Å^{-1}$

Table 4. BASIS Instrument Details[131]:

Elastic energy	2.08 meV
Bandwidth	+/- 100 μeV or +/- 200 μeV
Elastic Resolution	3.5 μeV
Q range	0.2 - 2.0 $Å^{-1}$

Chapter 3: Data Analysis

3.1 Fitting Routine

3.1.1 Bayesian Theory

In the words of von Neumann: "*With four parameters I can fit an elephant, and with five I can make him wiggle his trunk.*"[132] Fitting data involves judgement on whether additional parameters are necessary. Essentially there are two goals in mind: (1) obtaining lowest figure of merit, χ^2 and (2) using the least number of parameters. QENS fitting follows this χ^2 minimization procedure.[133] A probabilistic approach based on Bayesian theorem tests goodness of fit.[134, 135] This method yields a probability distribution function (PDF) relating fitted parameters to the figure of merit, χ^2 (Figure 15).

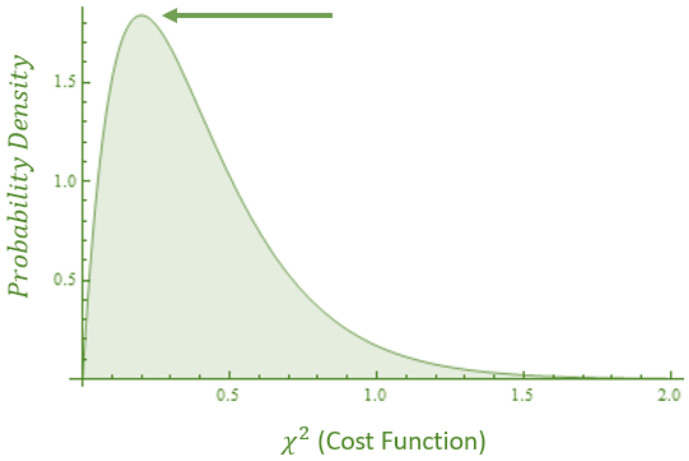

Figure 15. A Probability Distribution Function (PDF) plot. The relationship between probability and Chi-squared is shown. The arrow indicates the most probable set of parameters which are agreeable to the data.

There are three significant advantages of utilizing a Bayesian approach. First, parameter correlations are considered. Second, a PDF provides an overview of goodness of fit. Third, if the count rate is low, χ^2 can be redefined to allow for flexibility. In classical fitting, the degree of "truth" is related to how well a hypothesized model resembles raw data.[136, 137] A quantitative representation of this figure of merit, χ^2 is defined as the following[137]:

$$\chi^2 = \sum_{k=1}^{n} \frac{(H_K\{P_i\} - D_k)^2}{\sigma_k^2} \tag{14}$$

Where *n* is the number of experimental points, D_k is the experimental data, $H_K\{P_i\}$ is fitted values obtained from a mathematical model using P_i number of parameters, and σ_k is experimental error. The classic Levenberg-Marquadt algorithm aims to find local minimum χ^2 with no parameter correlations.[135] However, in Bayesian theory, parameter correlation is considered, and using probability notation we can write the following:

$$P(H_k \mid D_k) = \frac{P(D_k \mid H_k)P(H_k)}{P(D_k)} \tag{15}$$

Where $P(H_k \mid D_k)$ is the posterior, the probability that the hypothesis relates to the data. $P(D_k \mid H_k)$ is the likelihood that the hypothesis *well* describes data. $P(H_k)$ is the prior information that is available about the hypothesis. Finally, $P(D_k)$ is a normalization factor. This probabilistic approach allows one to find a *global* minimum χ^2 value and is thus a reasonable approach to data fitting.

Bayesian analysis is used by the MANTID software package[138] to fit all QENS spectra in this Thesis. MANTID implements an algorithm for Bayesian fitting called "FABADA: a Fitting Algorithm for Bayesian Analysis of Data."[139, 140] This algorithm utilizes the same

probability principles in order to answer the age old question of how many dynamic components exist in a QENS spectra.[141] Inspection of the χ^2 PDFs obtained this way enables model selection in a robust and quantitative manner.

Chapter 4: Cation dynamics in ethylammonium nitrate (EAN)

4.1 Fixed Window Elastic Scan (FWES)

A fixed window elastic scan (FWES) measures the onset of relaxation processes of all motions across the temperature range.[142] Such scans are useful because they can detect dynamic processes faster than the timescale of the instrument (at resolution = 1 μeV, this corresponds to ~10 ns) as well as phase changes in the material under study. The FWES for d_3-EAN as measured on the HFBS instrument is presented below (Figure 16).

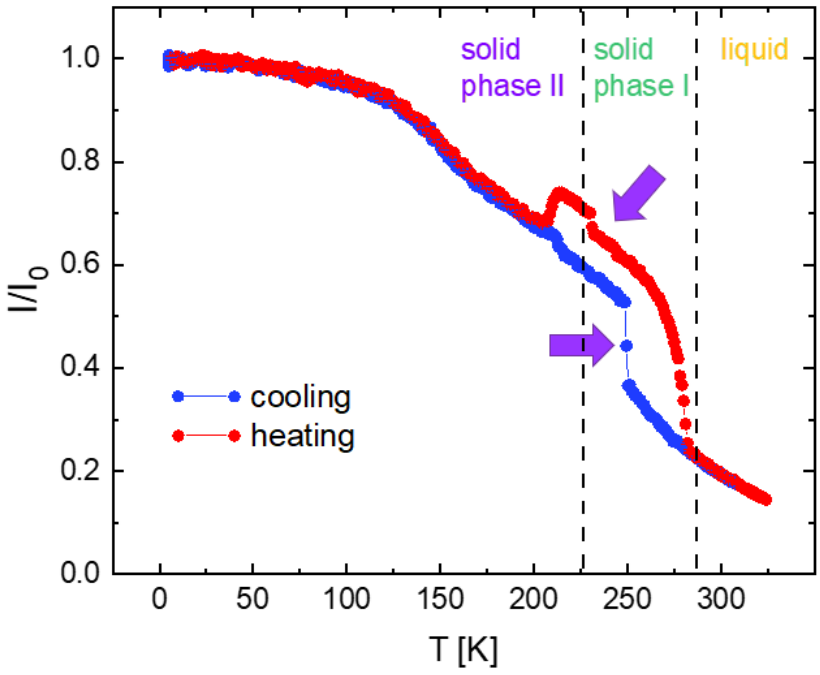

Figure 16. Temperature dependence of fixed window elastic scan (FWES) of d_3-EAN upon cooling and heating (1 K.min^{-1}) over all Q values. The change in intensity arises from EAN phase transitions, which leads to differences in total inelastic scattering and is consistent with a thermally-activated stochastic motion. Hysteresis in the two curves is likely a consequence of a super-cooling in the glassy phase (S2). Data was normalized against the lowest temperature value at T = 4 K. Arrows point to critical points in the transition curves.

Across the full temperature range, the normalized elastically scattered neutron intensity is measured with its *Q*-dependence.[142] The data for EAN was measured over an average of *Q* values with two thermal paths to affirm reversibility of the phase transitions. Intensity was normalized against data at the lowest temperature data set (T = 4 K). This is because all atomic and molecular motions are suspended at 4 K, and so elastic scattering is maximized, and inelastic scattering minimized. Data is recorded on both a "cooling curve" (308 K$\rightarrow$ 4 K), and then a heating curve (4 K$\rightarrow$ 308 K), at a rate of 1 K/min. Hysteresis is present between the two thermal paths, and is attributed to known supercooling in the EAN's amorphous phase (solid phase II).[8] Similar behavior has been noted in the QENS literature for other ionic liquids[91, 99] and glassy systems.[143]

Three phases are detected in the FWES scan; amorphous solid 2, crystalline solid 1, and the liquid phase. The number of phases, and critical temperatures are consistent with the phase diagram developed by Henderson et al.[144] In Figure 17, the phase transitions are marked by abrupt drops in elastic intensity and attributed to solid-solid ($T_{S1\rightarrow S2}$ = 229 K) and solid-liquid (T_m = 286 K) transition.[145] These values agree with differential scanning calorimetry (DSC) scans previously reported (Figure 17a).

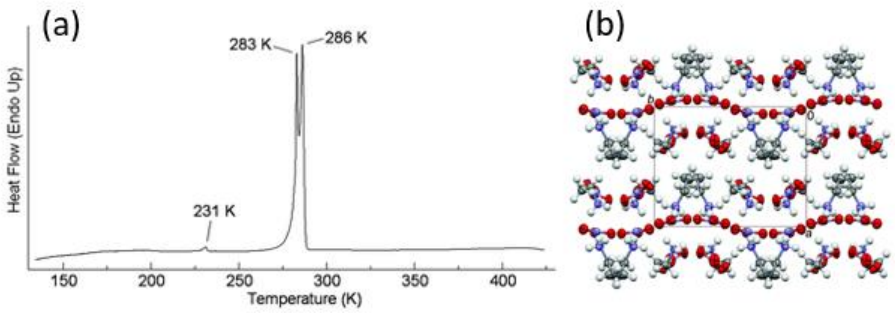

Figure 17. (a) DSC heating trace of EAN (1 K/min rate). The small bump at 231 K corresponds to a solid-solid phase transition, while the additional peak (T = 283 K) near the melting peak (T = 286 K) is believed to be another solid-solid transition. (b) Ion packing in the crystal structure of EAN. Adapted from.[144]

At maximum intensity (I/I_0 = 1), d_3-EAN is purely elastic; departure from this value denotes the onset of inelastic character that arises from ion motion. The data shows that dynamics are triggered at temperatures as low as ~ 100 K. This loss of elastic signal here is induced by methyl group (-CH_3) relaxation where neutrons detect methyl group protons rotating about a 3-fold symmetry axis. Both the linearity and modest slope of the FWES curves in this low temperature region (T < 100 K) are consistent with (-CH_3) relaxations reported for glassy systems[143, 146] and ILs.[91, 99] A closer examination of this data in Figure 18 shows good agreement with linear as predicted by the Lamb-Mossbauer effect.[143]

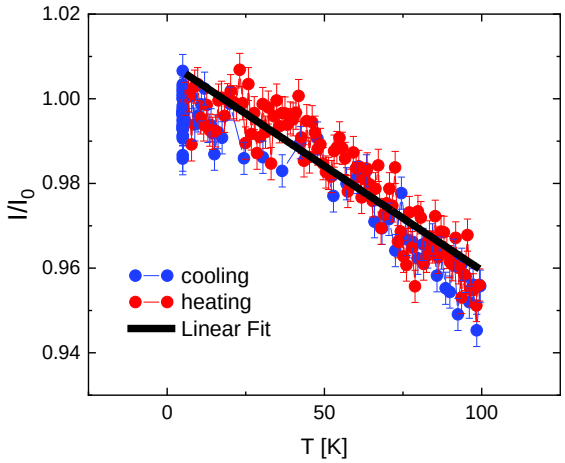

Figure 18. Snapshot of the temperature dependence of fixed window elastic scan (FWES) of d_3-EAN upon cooling and heating (1 $K \cdot min^{-1}$) over all Q values. Values are shown < 100 K to highlight the linear dependence of the Lamb-Mossbauer effect.

4.2 Low Temperature dynamics in [EAN]

4.2.1 Elastic Incoherent Structure Factor (EISF)

Elastic Incoherent Structure Factor (EISF) is a measure of the elastic contribution to total scattering in QENS experiments.[90] It is defined as:

$$EISF(Q) = \frac{A_0(Q)}{A_0(Q) + A_1(Q)} \tag{16}$$

Where $A_0(Q)$ and $A_1(Q)$ correspond to elastic and quasi-elastic character in the sample respectively, a visual representation of this in the QENS spectra is shown below (Figure 19).

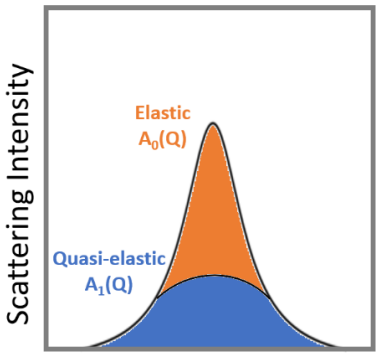

Figure 19. QENS spectra divided into its elastic and quasi-elastic components.

Unlike FWES that is sensitive to all motion, EISF detects localized motions occurring within a certain geometrical spatial confinement. EISF can be thought of as the probability that a particle (in this case an atom or ion) is found within the same volume of space over a given increment time $t_0 \rightarrow t_1$. Since it is *Q*-dependent, EISF provides information on the spatial region accessible of motions at different length-scales. EISF data for EAN is presented in Figure 20. Elastic intensity rapidly decreases with increasing *Q;* as *Q* is measured in reciprocal angstroms ($Å^{-1}$), this indicates that elastic intensity and therefore motion is (1) small for small length scales around the size of EAN ions and (2) high at length-scales much larger than ion pair or solvent nanostructure.

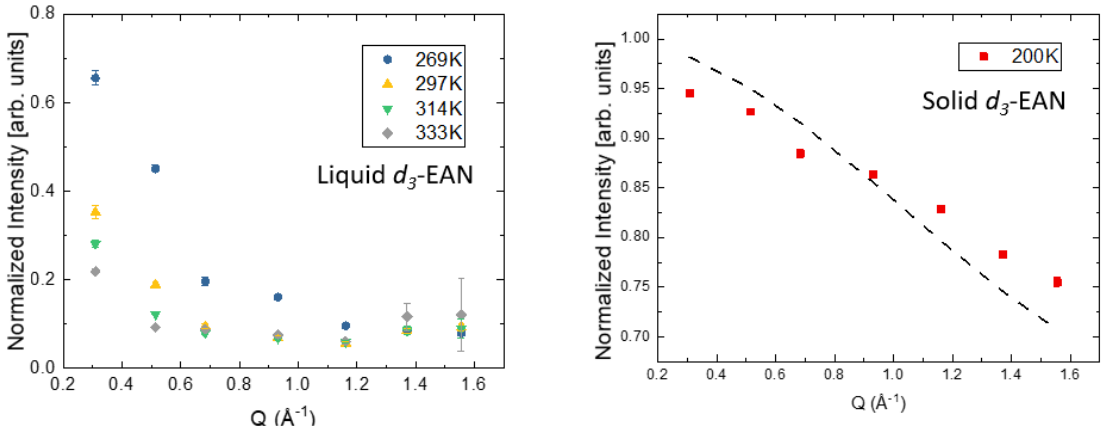

Figure 20. *Q*-dependence of Elastic Incoherent Structure Factor (EISF) over the liquid (left) and solid (right) phase. The dashed curve is predicted EISF based on eq 17 for a three-fold methyl group rotation. Temperatures were measured below and above the melting point of EAN (T_m = 285 K). In the liquid phase, there is sharp decrease in elastic intensity. Error bars represent one standard deviation.

Using standard protocols for EISF analysis, the intensity has been normalized by dividing each intensity value by the lowest available data set. For liquid phase data (Figure 20a), Q = 0.6830 Å^{-1} marks an important dynamic transition; signal intensity is pronounced at low scattering angles Q < 0.6830 Å^{-1} whereas at Q values Q > 0.6830, intensity is essentially invariant. This Q value is significant as is coincides with the pre-peak position in neutron diffraction studies of EAN (c.f. Figure 4) and corresponds to a distance of twice the ion pair size from the Bragg equation (2π / 0.6830 Å^{-1} = 10 Å). This suggests that the critical length scale of EAN nanostructure is key to understanding different dynamic processes in the IL. Data at 0.6830 Å^{-1} < Q < 1.712 Å^{-1} must relate to the cation motions confined within the local segregation of sponge-like nanostructure. Conversely, EISF data Q < 0.6830 Å^{-1} arises from cations motion beyond the polar/apolar segregation. As shown in Figure 20,

this change in intensity becomes more abrupt with increasing temperature; in every case the normalized EISF intensity is highest for 269 K than 333 K, indicating that the ion motion is enhanced at higher temperatures.

Figure 20 also shows EISF data for solid EAN at 200 K. Using a model developed by Kofu et al.[101], good fits to methyl rotations in the solid phase are obtained using the expression:

$$A_0(Q) = \frac{5}{8} + \frac{3}{8}\frac{1}{3}\left[1 + 2j_0\left(\sqrt{\frac{8}{3}}Qd\right)\right] \quad (17)$$

Where (5/8) represents ρ or the fraction of immobile protons on the cation at this temperature and (3/8) is the fraction of mobile protons ρ_{mobile} on the methyl end group (CH_3). (1/3) defines the probability of a proton being on a jump site at equilibrium, and brackets hold the expression for elastic character $A_0(Q)$. *d* is the jump site distance corresponding to the physical distance between hydrogen and carbon atoms, a C-H bond ~ 1.09 Å. Schematically, the equation is illustrated in Figure 21.

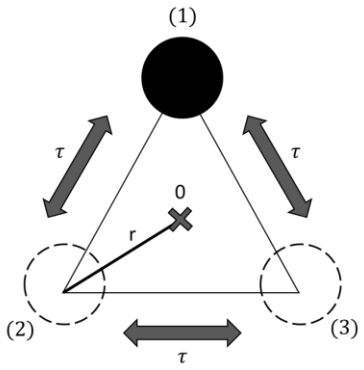

Figure 21. Schematic of a three-fold symmetry of CH_3 proton rotation about a single axis to model EISF data in EAN's solid phase. Adapted from.[90]

Since ammonium group is deuterated -ND_3, the motion and loss of elastic intensity seen in the low temperature regime must arises is solely from the contribution of methyl group protons. As an aside, similar fitting cannot be performed for CH_3 rotations at liquid EAN temperatures because the dynamics of the methyl group cannot be isolated from other motions.

4.3 Liquid State Dynamics

4.3.1 Dynamic Structure Factor S(Q)

Figure 22 and 23 show *Q*-dependent and temperature-dependent dynamic structure factor S(Q, ω) respectively for d_3-EAN on the HFBS instrument (Energy Bandwidth = ± 50 μeV). The *Q*-dependence of the dynamic incoherent structure factor is shown in Figure 22 at fixed T = 200 K. In Figure 23, temperature is varied, while Q remains invariant at 0.3085 $Å^{-1}$. Insets in both graphs show maximum intensities of each peak. Many other similar spectra for d_3-EAN at different *Q*-values or temperatures are presented in the Appendix, including corresponding measurements on BASIS.

The S(Q, ω) captures key quantitative dynamic information of the d_3-EAN cation. As presented in Figures 22 and 23, each individual QENS peak shares two characteristics: (1) a narrow central peak indicating strong elastic signal and (2) a broad peak base that denotes quasi-elastic character. The relative peak intensity and peak broadness vs. sharpness thus reflects the different dynamic character of the QENS signal and is the focus of data fitting detailed below. Peak broadening adduces dynamic processes that transpire within the accessible energy windows of the instrument.

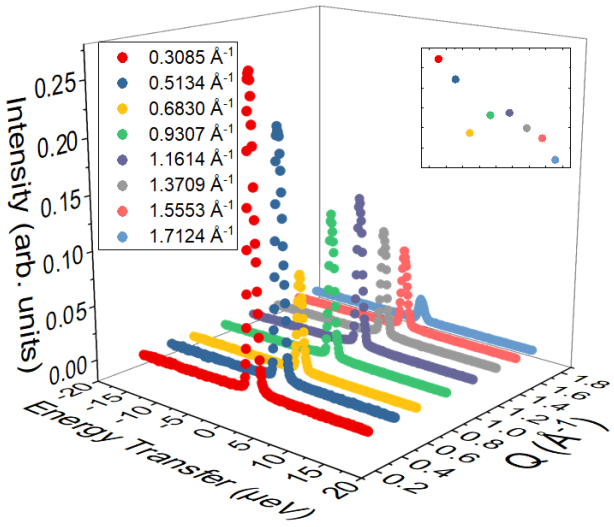

Figure 22. Raw unfitted Dynamic Structure Factor S(*Q*) of d3-EAN at *T* = 200 K. The data is taken on the HFBS instrument from a *Q* range of 0.3085 Å^{-1} < *Q* < 1.7124 Å^{-1}. An unexpected dip in the intensity of the spectra occurs at Q = 0.6830 Å^{-1} and 0.9307 Å^{-1}, indicating a convolution of the first sharp diffraction peak measured in S(q) in Ref .[61] Inset shows the relative peak intensities.

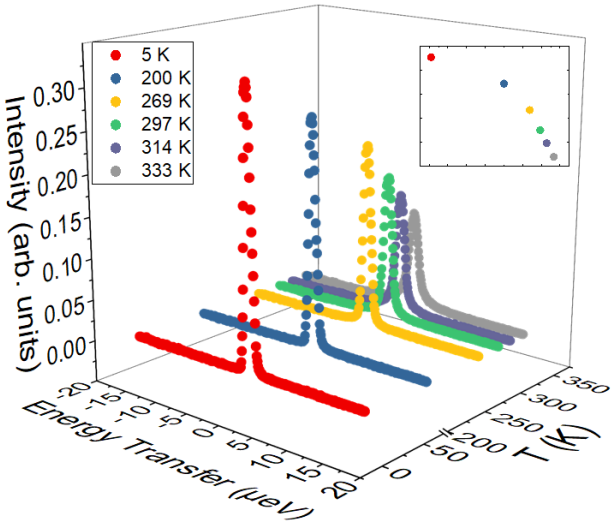

Figure 23. Raw unfitted Dynamic Structure Factor S(*Q*) of EAN at *Q* = 0.3085 Å^{-1}. The data is taken on the HFBS instrument from a *T* range of 200K < *T* < 333K. There is temperature dependence of intensity and line broadness, typical of QENS structure factors. Inset shows the relative peak intensities.

In general, the peak broadens in both Figure 22 and Figure 23 from 0.3085 to 1.7124 $Å^{-1}$ or from 5 K to 333 K. This indicates faster motions in EAN as (1) S(Q, ω) focuses structure at the level of atomic and functional group motions instead of ions, ion pairs or EAN nanostructure and (2) the sample is heated from solid → liquid phase. In other words, as expected, stochastic processes are faster and incident neutrons exchange more energy with EAN at higher temperature or when restricted to cations within single apolar domains.

A similar and related trend is noted in peak intensity. In almost every case, max peak height decreases from 0.3085 to 1.7124 $Å^{-1}$ or from 5 K to 333 K. This suggests that elastic intensity decreases due to increased neutron-nuclei interaction.

The dip in Figure 22 indicates that the first sharp diffraction peak measured in EAN's *S(q)* [61] is convoluted in the S(Q, ω) data precisely because measurements were performed on the d_3-EAN system. This suggests EAN's dynamics undergo a transition at the length-scale associated with nanostructure.[61]

Using standard fitting procedures, each spectra in the QENS data was fitted with MANTID software package[138]; fitting multiple *S*(Q, ω) with the same dynamic model simultaneously affords confidence in the extracted diffusion parameters. From the energy resolution of HFBS, quasi-elastic line broadening can be attributed to a single dynamic event. The raw data was fitted to the following dynamic structure factor:

$$S(Q,\omega) = R(Q,\omega) \otimes [\delta(Q) + L(Q,\omega)] + bg \qquad (18)$$

Where $R(Q,\omega)$ is the instrument resolution, $\delta(Q)$ is the delta function accounting for motions too slow to be resolved, $L(Q,\omega)$ is a Lorentzian function, $\otimes$ is the convolution operator, and *bg* is a linear background accounting for motion faster than accessible energy

range. The total fit line is a composite function of only these parameters. A representative fit for d_3-EAN measured at T = 296 K and Q = 0.5314 Å^{-1} is shown in Figure 24; diffusion values presented in this Thesis are derived from these fits for all S(Q, ω) across each T- and Q-value in Figures 22 & 23, binned by temperature.

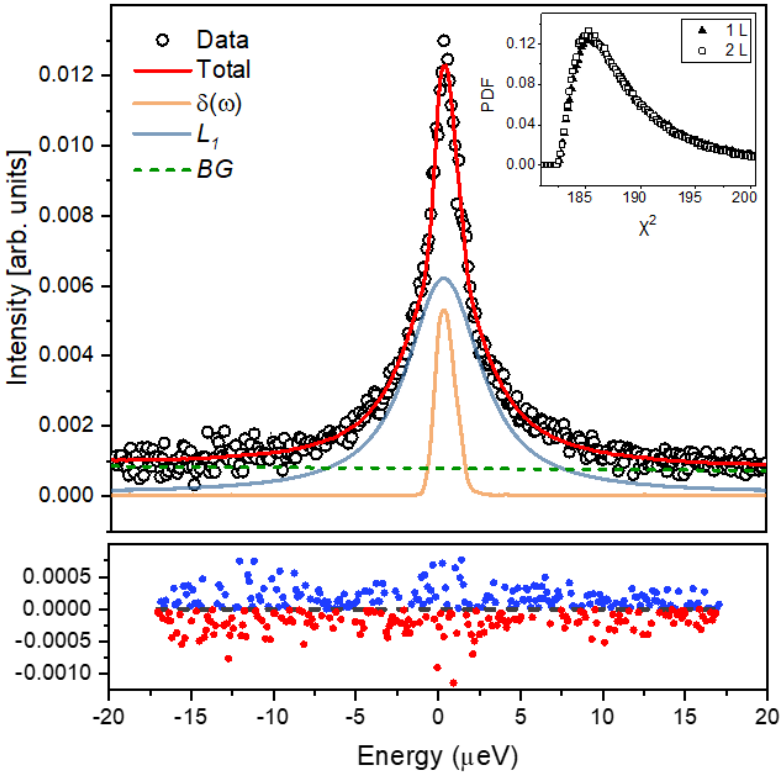

Figure 24. Upper Panel: A representative example of the fitted dynamic structure factor S(Q, ω) of EAN measured at T = 296 K and Q = 0.5314 Å^{-1}. (symbols). The data is described by a dynamic process associated with a Lorentzian component (solid blue) of which the total fitting line (solid red) is composed of. Fit was performed in accordance with eq 18, details are further discussed in the text. Inset: Probability density function (PDF) for the figure of merit χ^2 for a 1 Lorentzian versus 2 Lorentzian fit as determined through Bayesian analysis. This demonstrates that 1 Lorentzian is sufficient to describe data without penalizing goodness of fit. In the lower panel, positive (blue) and negative (red) residuals between the fit function and raw data are highlighted.

Excellent fits are obtained across all S(Q, ω) spectra. This is indicated by the unbiased distribution of residuals from the fit across blue and red data in Figure 24. Notably, only a single Lorentzian function is required to adequately model the data. This is important as from equation 19, the number of Lorentzian functions indicate the number of discrete dynamic events that transpire in the liquid:

$$S(Q,\omega) = R(Q,\omega) \otimes [\delta(Q) + L_1(Q,\omega) + L_2(Q,\omega) + ...] + bg \tag{19}$$

Systematic Bayesian analysis of the QENS spectra show that a single and dual Lorentzian fit are indistinguishable from PDF versus χ^2 plot (c.f. inset Figure 24). Here, the most probable value of the χ^2 is near identical to each other. Higher order modelling using three or more Lorentzian functions also did not improve fit quality. This suggests a single cationic diffusion process suffices to capture all the dynamic processes in EAN fluid. The line-width analysis of the fitted QENS peaks for d_3-EAN is detailed in the next section.

4.3.2 Line-width Analysis

In Figure 25 the QENS line widths (half-width half maximum, HWHM) of liquid d_3-EAN were plotted as a function of Q^2. HWHM is used in many fields to measures broadness of peaks without excess bias from peak height or base.

HWHM data was fitted with a simple Fickian Law, represented by solid lines:

$$\Gamma(Q) = \hbar D_s Q^2 \tag{20}$$

Here, D_s is the self-diffusion coefficient, Q is momentum transfer, and $\hbar$ is reduced Planck's constant. A linear increase in HWHM is noted as a function of Q^2. This confirms that the dynamic process in EAN is best described as Fickian across all T and Q values in

the liquid phase, as previously described in Figure 13. Many examples of Fickian diffusion in ILs has been reported in the literature.[147, 148] Interestingly, this contrasts with QENS data fitting that employ jump diffusion models for ILs.[95-100] On the HFBS instrument, we see no evidence of line-widths saturating at high *Q* that would be expected if EAN cations showed a hopping process at very short length-scales. In addition, Figure 25 shows that the slope of HWHM line-widths increase as a function of temperature. This again denotes faster dynamics at higher temperature.

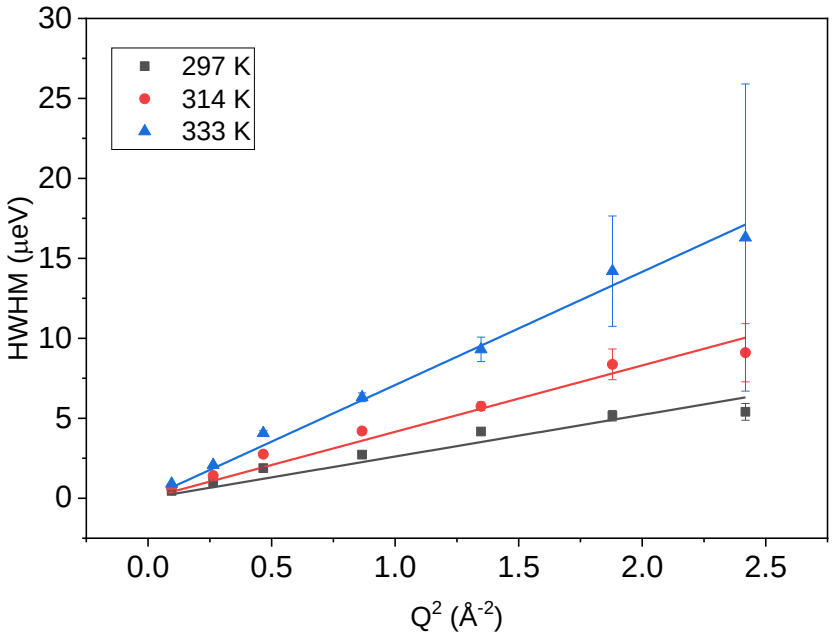

Figure 25. Fit results of the temperature dependence for half-width half maximum $\Gamma_{1/2}$ as a function of *Q* at liquid phase temperatures (> 285 K). Solid lines were fitted with eq 20 describing a Fickian model. Details of fitting can be found in the text.

The temperature dependence of diffusion coefficient (*D*) can be extracted from this model using the celebrated Arrhenius equation:

$$D = D_0 \exp(-E_A / RT) \quad (21)$$

Where R denotes the gas constant 8.314 J/(mol·K), E_A is the activation energy for the corresponding diffusional process, D_0 is known as the pre-exponential factor, and T is temperature.

From the fitting results, an activation energy of E_A = 21.6 ± 0 kJ/mol is obtained for EAN. This value for activation energy is larger than the aprotic IL C_4mimCl (E_A = 10.9 kJ/mol) which was also reported to follow Fick's Law.[147] Furthermore, it is also larger than the activation energies of jump diffusion aprotic[96, 102] and protic[99, 100] ILs, and for intramolecular rotational energy barrier of *n*-alkanes (13 - 15 kJ/mol).[149] This is likely a consequence of EAN's nanostructure,[61] which provides a high thermal barrier for ion motion in the bulk. Notably, similar relationship between nanostructure and bulk thermal conductivity has been determine for bulk heat transfer.[150, 151]

The diffusion coefficient (D) for EAN can also be calculated and it is plotted in isolation in Figure 26 and compared to other liquids and condensed phases in Figure 27. The long range cation diffusion in d_3-EAN is slower and smaller than other ILs measured using QENS, yet not as slavish compared to the liquid crystal 8CB. This is plausibly explained by the pronounced solvent nanostructure in EAN, which inhibits rapid ion diffusion in the bulk phase, although we cannot make an unequivocal determination.

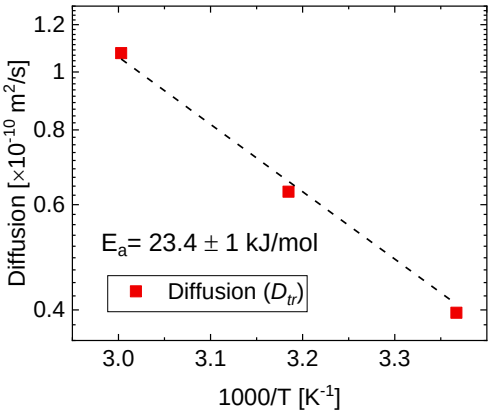

Figure 26. Arrhenius Plot of the diffusion coefficient D (red symbols) describing long-range diffusion as a function of the inverse temperature. Symbols denote the values of *D* obtained for the three liquid phase temperatures (297, 314 and 333 K respectively). Dashed line represents a fit modeled by the Arrhenius equation in eq 21. Activation energy of the translational process is Ea = 23.4 ± 1 kJ/mol.

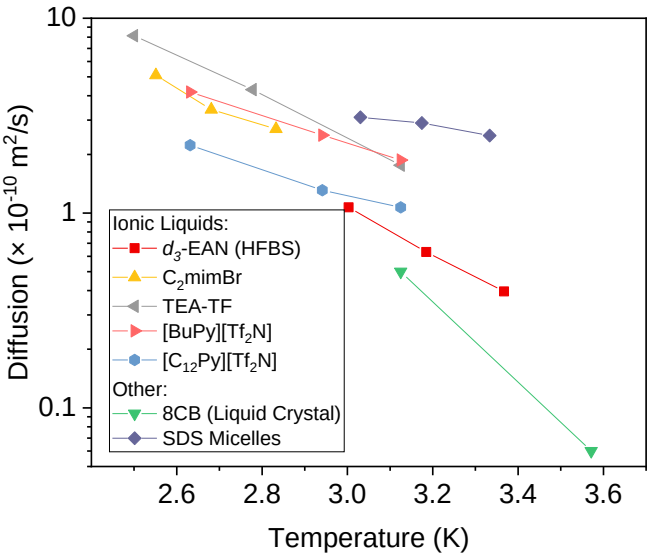

Figure 27. Arrhenius Plot of the long-range translation diffusion of several liquid systems. The data presented in this Thesis is shown for comparison. Literature values depicted for C_2mimBr,[152] TEA-TF,[99] [BuPy][Tf_2N],[98] [C_{12}Py][Tf_2N],[98] 8CB,[153] and SDS micelles.[154]

Chapter 5: Conclusions and Outlook

In this Thesis, the bulk ion dynamics of the oldest and most famous protic ionic liquid ethylammonium nitrate (EAN) is examined using quasi elastic neutron scattering (QENS). For the first time, neutrons have been employed to probe nanoscale structural and dynamic correlations in this IL across all three phases. The key advantage of QENS is that when paired with H/D isotopic substitution, the wide temperature, length and energy scale of neutrons allow the characterization of many different dynamic processes in the bulk, from methyl group rotations to long range cation diffusion. The good fits to the QENS data was obtained using analytical models and Bayesian statistics, enabling new insight into EAN's ion dynamics:

(1) Methyl group rotations are the simpliest dynamic motion present in EAN, and first appear in the QENS signal at ~100 K in the solid phase. These rotations are well described by the Kofu et al.'s model,[101] and is similar to findings in many liquids, ILs and condensed phases.

(2) The measured dynamic structure factor S(Q, ω) of EAN showed temperature (*T*) and length-scale (*Q*) dependence. The length-scale (*Q*) dependence is most interesting, as at Q = 0.6830 Å^{-1}, the bulk pre-peak that reflects long range solvent nanostructure is convoluted into the S(Q, ω). This leads to a dynamics crossover at this length scale in the elastic incoherent structure factor, meaning that the sponge-like nanostructure restricts ion motion within the segregation of charged and uncharged domains in the bulk.

(3) Bayesian statistical models are a powerful and underused approach to fitting QENS data. Using the protocols described in this thesis, it was found that d_3-EAN S(Q, ω) can be

explained by a single dynamic component for the long-range cationic translational diffusion. This diffusion is Fickian, and self-diffusion coefficient was determined to be 3.96×10^{-11} m^2/s at 298 K. In comparison, most other ILs and glassy systems follow a jump diffusion model and typically have faster diffusion coefficients. The long-range cation diffusion was confirmed to follow Arrhenius behavior, and the subsequent activation energy $E_A = 21.6 \pm 0$ kJ/mol was also higher than the same process in similar systems.

Together, these results highlight the utility of neutron scattering to examine nanoscale dynamics of IL ions whilst simultaneously accounting for self-assembled morphology. Future work should extend this using H/D isotopic substitution to many protic and aprotic ILs, as well as their mixtures with other solvents. There is likely more dynamic information to be uncovered for EAN; as shown in Figure 28, the d_5-EAN contrast could be measured using QENS to focus on the motion of exchangeable ammonium protons. As neutrons provide a powerful tool to probe into hydrogen-rich materials, systematic deuteration will reveal the mechanism of charge transport in the bulk, whether it proceeds via ion translation, proton diffusion, or a combination of these.

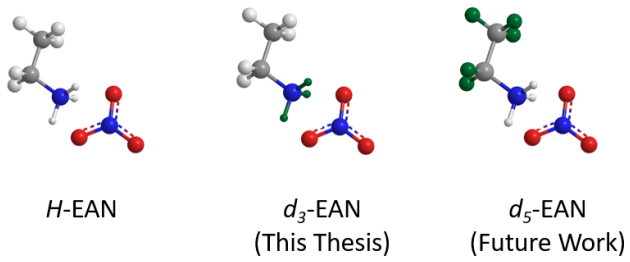

Figure 28. Possible contrasts of EAN.

Pulse-field gradient spin-echo (PFGSE) NMR is another promising technique to explore in the future. For example, $H^{15}NO_3$ using ^{15}N nuclei is ripe for experiments, enabling NO_3^- anion diffusion to be tracked and compared to the QENS data described here for cation diffusion. Furthermore, as NMR dynamics are in a different order of magnitude (millisecond) than QENS (sub-pico, sub-nano) this will give more information on diffusion coefficients. Another step would be to incorporate MD simulations into the study.[155] This would give access to the dynamic structure factor $S(Q,\omega)$ and computational and experimental spectra can be compared.

Chapter 6: Bibliography

1. C. Reichardt and T. Welton, *Solvents and solvent effects in organic chemistry*, Wiley-VCH, Weinheim, 4th edn., 2011.
2. C. Reichardt, *Org. Res. Process & Develop.*, 2007, **11**, 105.
3. G. Wypych and J. Wypych, *Handbook of Solvents*, ChemTec Publishing, 2001.
4. R. A. Sheldon, *Green Chem.*, 2017, **19**, 18-43.
5. M. J. Earle and K. R. Seddon, in *Clean Solvents*, American Chemical Society, 2002, vol. 819, ch. 2, pp. 10-25.
6. R. D. Rogers and K. R. Seddon, *Science*, 2003, **302**, 792-793.
7. R. Hayes, G. G. Warr and R. Atkin, *Chem. Rev. (Washington, DC, U. S.)*, 2015, **115**, 6357-6426.
8. C. A. Angell, N. Byrne and J.-P. Belieres, *Acc. Chem. Res.*, 2007, **40**, 1228-1236.
9. T. L. Greaves and C. J. Drummond, *Chem. Rev.*, 2008, **108**, 206-237.
10. J. Dupont, *J. Braz. Chem. Soc.*, 2004, **15**, 341-350.
11. T. L. Greaves and C. J. Drummond, *Chem. Soc. Rev.*, 2013, **42**, 1096-1120.
12. E. W. J. Castner, C. J. Margulis, M. Maroncelli and J. F. Wishart, *Annu. Rev. Phys. Chem.*, 2011, **62**, 85-105.
13. H. Weingärtner, *Angew. Chem. Int. Ed.* , 2008, **47**, 654 - 670.
14. R. Hayes, G. G. Warr and R. Atkin, *Phys. Chem. Chem. Phys.*, 2010, **12**, 1709–1723.
15. P. A. Z. Suarez, S. Einloft, J. E. L. Dullius, R. F. de Souza and J. Dupont, *J. Chim. Phys.*, 1998, **95**, 1626.
16. J. S. Wilkes and M. J. Zaworotko, *J. Chem. Soc., Chem. Commun.*, 1992, 965.
17. K. M. Dieter, C. J. Dymek, N. E. Heimer, J. W. Rovang and J. S. Wilkes, *J. Am. Chem. Soc.*, 1988, **110**, 2722-2726.
18. H. H. Paradies and F. Habben, *Acta Cryst. Sect. C*, 1993, **49**, 744-747.
19. R. G. Laughlin, *The Aqueous Phase Behavior of Surfactants* Academic Press, 1996.
20. H. Satoshi, O. Ryosuke and H. Hiro-o, *Chemistry Letters*, 2003, **32**, 498-499.
21. K.-S. Lee, J. S. Spendelow, Y.-K. Choe, C. Fujimoto and Y. S. Kim, *Nature Energy*, 2016, **1**, 16120.
22. H. K. Stassen, R. Ludwig, A. Wulf and J. Dupont, *Chemistry – A European Journal*, 2015, **21**, 8324-8335.
23. S. T. van der Post, J. Hunger, M. Bonn and H. J. Bakker, *The Journal of Physical Chemistry B*, 2014, **118**, 4397-4403.
24. H. Chen and E. Ruckenstein, *The Journal of Physical Chemistry B*, 2015, **119**, 12671-12676.
25. N. Bjerrum, *Danske Videnskab. Selsk. Mat.-Fys. Medd.*, 1926, **7**, 1.
26. B. A. D. Neto, E. C. Meurer, R. Galaverna, B. J. Bythell, J. Dupont, R. G. Cooks and M. N. Eberlin, *J. Phys. Chem. Lett.*, 2012, **3**, 3435-3441.
27. J. P. Armstrong, C. Hurst, R. G. Jones, P. Licence, K. R. J. Lovelock, C. J. Satterley and I. J. Villar-Garcia, *Phys. Chem. Chem. Phys.*, 2007, **9**, 982-990.
28. J. P. Leal, J. M. S. S. Esperanea, M. E. Minas da Piedade, J. N. Canongia Lopes, L. P. N. Rebelo and K. R. Seddon, *J. Phys. Chem. A*, 2007, **111**, 6176-6182.
29. H. Weingärtner, A. Knocks, W. Schrader and U. Kaatze, *The Journal of Physical Chemistry A*, 2001, **105**, 8646-8650.
30. S. Schrödle, G. Annat, D. R. MacFarlane, M. Forsyth, R. Buchner and G. Hefter, *Chemical Communications*, 2006, DOI: 10.1039/B602209J, 1748-1750.

31. D. A. Turton, T. Sonnleitner, A. Ortnew, M. Walther, G. Hefter, K. R. Seddon, S. Stana, N. Plechkova, R. Buchner and K. Wynne, *Faraday Discuss.*, 2012, **154**, 145-153.
32. H. Weingärtner, *Curr. Opin. Colloid Interface Sci.*, 2013, **18**, 183-189.
33. R. M. Lynden-Bell, *Phys. Chem. Chem. Phys.*, 2010, **12**, 1733-1740.
34. A. A. Lee, D. Vella, S. Perkin and A. Goriely, *The Journal of Physical Chemistry Letters*, 2015, **6**, 159-163.
35. K. Ueno, H. Tokuda and M. Watanabe, *Phys. Chem. Chem. Phys.*, 2010, **12**, 1649-1658.
36. D. F. Evans, S.-H. Chen, G. W. Schriver and E. M. Arnett, *Journal of the American Chemical Society*, 1981, **103**, 481-482.
37. K. Fumino, A. Wulf and R. Ludwig, *Angew. Chem. Int. Ed.*, 2009, **48**, 3184.
38. K. Fumino, E. Reichert, K. Wittler, R. Hempelmann and R. Ludwig, *Angew. Chem. Int. Ed.*, 2012, **51**, 6236-6240.
39. K. Fumino, S. Reimann and R. Ludwig, *Phys. Chem. Chem. Phys.*, 2014, **16**, 21903-21929.
40. S. Chen, S. Zhang, X. Liu, J. Wang, J. Wang, K. Dong, J. Sun and B. Xu, *Phys. Chem. Chem. Phys.*, 2014, **16**, 5893-5906.
41. F. C. Gozzo, L. S. Santos, R. Augusti, C. S. Consorti, J. Dupont and M. N. Eberlin, *Chem. Eur. J.* , 2004, **10**, 6187-6193.
42. R. Bini, O. Bortolini, C. Chiappe, D. Pieraccini and T. Siciliano, *J. Phys. Chem. B*, 2006, **111**, 598-604.
43. C. S. Consorti, P. A. Z. Suarez, R. F. de Souza, R. A. Burrow, D. H. Farrar, A. J. Lough, W. Loh, L. H. M. da Silva and J. Dupont, *J. Phys. Chem. B*, 2005, **109**, 4341-4349.
44. B. A. DaSilveira Neto, L. S. Santos, F. M. Nachtigall, M. N. Eberlin and J. Dupont, *Angew. Chem.*, 2006, **118**, 7409-7412.
45. P. J. Dyson, I. Khalaila, S. Luettgen, J. S. McIndoe and D. Zhao, *Chem. Commun.*, 2004, **0**, 2204-2205.
46. S. Dorbritz, W. Ruth and U. Kragl, *Advanced Synthesis & Catalysis*, 2005, **347**, 1273-1279.
47. D. F. Kennedy and C. J. Drummond, *J. Phys. Chem. B*, 2009, **113**, 5690.
48. S. A. Katsyuba, P. J. Dyson, E. E. Vandyukova, A. V. Chernova and A. Vidiš, *Helvetica Chimica Acta*, 2004, **87**, 2556-2565.
49. Y. Umebayashi, T. Mitsugi, K. Fujii, S. Seki, K. Chiba, H. Yamamoto, J. N. Canongia Lopes, A. A. H. Pádua, M. Takeuchi, R. Kanzaki and S.-i. Ishiguro, *J. Phys. Chem. B*, 2009, **113**, 4338-4346.
50. Y. Umebayashi, S. Mori, K. Fujii, S. Tsuzuki, S. Seki, K. Hayamizu and S.-i. Ishiguro, *J. Phys. Chem. B*, 2010, **114**, 6513-6521.
51. R. W. Berg, M. Deetlefs, K. R. Seddon, I. Shim and J. M. Thompson, *J. Phys. Chem. B*, 2005, **109**, 19018-19025.
52. C. J. Johnson, J. A. Fournier, C. T. Wolke and M. A. Johnson, *J. Chem. Phys.*, 2013, **139**, 224305
53. Y. Umebayashi, T. Fujimori, T. Sukizaki, M. Asada, K. Fujii, R. Kanzaki and S.-i. Ishiguro, *J. Phys. Chem. A*, 2005, **109**, 8976-8982.
54. Y. Wang and G. A. Voth, *Journal of the American Chemical Society*, 2005, **127**, 12192-12193.
55. Y. Wang and G. A. Voth, *J. Phys. Chem. B*, 2006, **110**, 18601-18608.
56. S. M. Urahata and M. C. C. Ribeiro, *The Journal of Chemical Physics*, 2004, **120**, 1855-1863.
57. U. Schröder, J. D. Wadhawan, R. G. Compton, F. Marken, P. A. Z. Suarez, C. S. Consorti, R. F. de Souza and J. Dupont, *New J. Chem.*, 2000, **24**, 1009.
58. A. Triolo, O. Russina, B. Fazio, R. Triolo and E. Di Cola, *Chem. Phys. Lett.*, 2008, **457**, 362-365.

59. Y. Wang and G. A. Voth, *J. Am. Chem. Soc.*, 2005, **127**, 12192-12193.
60. H. Tanaka, *Faraday Discuss.*, 2013, **167**, 9-76.
61. R. Hayes, S. Imberti, G. G. Warr and R. Atkin, *Phys. Chem. Chem. Phys.*, 2011, **13**, 3237-3247.
62. T. L. Greaves, D. F. Kennedy, S. T. Mudie and C. J. Drummond, *J. Phys. Chem. B*, 2010, **114**, 10022-10031.
63. A. Triolo, O. Russina, H. J. Bleif and E. DiCola, *J. Phys. Chem. B*, 2007, **111**, 4641-4644.
64. H. K. Kashyap, C. S. Santos, H. V. R. Annapureddy, N. S. Murthy, C. J. Margulis and J. E. W. Castner, *Faraday Discussions*, 2012, **154**, 133-143.
65. R. Hayes, S. Imberti, G. G. Warr and R. Atkin, *The Journal of Physical Chemistry C*, 2014, **118**, 13998-14008.
66. R. Hayes, S. Imberti, G. G. Warr and R. Atkin, *Phys. Chem. Chem. Phys.*, 2011, **13**, 13544.
67. J. C. Araque, J. J. Hettige and C. J. Margulis, *J. Phys. Chem. B*, 2015, **119**, 12727-12740.
68. O. Russina, A. Triolo, L. Gontrani, R. Caminiti, D. Xiao, L. G. H. Jr, R. A. Bartsch, E. L. Quitevis, N. Plechkova and K. R. Seddon, *J. Phys.: Condens. Matter*, 2009, **21**, 424121.
69. C. Hardacre, J. D. Holbrey, C. L. Mullan, T. G. A. Youngs and D. T. Bowron, *J. Chem. Phys.*, 2010, **133**, 074510.
70. C. S. Santos, N. S. Murthy, G. A. Baker and E. W. C. Jr., *The Journal of Chemical Physics*, 2011, **134**, 121101.
71. H. V. R. Annapureddy, H. K. Kashyap, P. M. De Biase and C. J. Margulis, *J. Phys. Chem. B*, 2010, **114**, 16838-16846.
72. R. Hayes, S. Z. El Abedin and R. Atkin, *J. Phys. Chem. B*, 2009, **113**, 7049.
73. R. Hayes, S. Imberti, G. G. Warr and R. Atkin, *Angew. Chem. Int. Ed.*, 2013, **52**, 4623-4627.
74. T. Ishida and H. Shirota, *J. Phys. Chem. B*, 2012, **117**, 1136-1150.
75. P. Yang, G. A. Voth, D. Xiao, L. G. Hines, R. A. Bartsch and E. L. Quitevis, *J. Chem. Phys.*, 2011, **135**, 034502.
76. S. M. Urahata and M. C. C. Ribeiro, *The Journal of Chemical Physics*, 2005, **122**, 024511.
77. Z. Hu, X. Huang, H. V. R. Annapureddy and C. J. Margulis, *The Journal of Physical Chemistry B*, 2008, **112**, 7837-7849.
78. H. Shirota and E. W. Castner, *The Journal of Physical Chemistry A*, 2005, **109**, 9388-9392.
79. F. Bardak, D. Xiao, L. G. Hines, P. Son, R. A. Bartsch, E. L. Quitevis, P. Yang and G. A. Voth, *ChemPhysChem*, 2012, **13**, 1687-1700.
80. H. I. Shirota, T. , *J. Phys. Chem. B*, 2011, **115**, 10860−10870.
81. D. A. Turton, J. Hunger, A. Stoppa, G. Hefter, A. Thoman, M. Walther, R. Buchner and K. Wynne, *Journal of the American Chemical Society*, 2009, **131**, 11140-11146.
82. R. A. Marcus, *Reviews of Modern Physics*, 1993, **65**, 599-610.
83. Z.-P. Zheng, W.-H. Fan, S. Roy, K. Mazur, A. Nazet, R. Buchner, M. Bonn and J. Hunger, *Angew. Chem. Int. Ed.*, 2014, **54**, 687.
84. I. Ohmine and H. Tanaka, *Chemical Reviews*, 1993, **93**, 2545-2566.
85. D. Laage and J. T. Hynes, *Science*, 2006, **311**, 832-835.
86. J. Hunger, T. Sonnleitner, L. Liu, R. Buchner, M. Bonn and H. J. Bakker, *J. Phys. Chem. Lett.*, 2012, **3**, 3034-3038.
87. R. Richert and C. A. Angell, *The Journal of Chemical Physics*, 1998, **108**, 9016-9026.
88. M. Anouti, M. Caillon-Caravanier, C. Le Floch and D. Lemordant, *The Journal of Physical Chemistry B*, 2008, **112**, 9412-9416.
89. W. Xu, E. I. Cooper and C. A. Angell, *The Journal of Physical Chemistry B*, 2003, **107**, 6170-6178.

90. M. Bée, *Quasielastic neutron scattering: principles and applications in solid state chemistry, biology, and materials science*, Adam Hilger, Bristol, Eng. ; Philadelphia, 1988.
91. A. Triolo, O. Russina, V. Arrighi, F. Juranyi, S. Janssen and C. M. Gordon, *J. Chem. Phys.*, 2003, **119**, 8549-8557.
92. A. Triolo, O. Russina, C. Hardacre, M. Nieuwenhuyzen, M. A. Gonzalez and H. Grimm, *The Journal of Physical Chemistry B*, 2005, **109**, 22061-22066.
93. M. L. Hoarfrost, M. Tyagi, R. A. Segalman and J. A. Reimer, *J. Phys. Chem. B*, 2012, **116**, 8201-8209.
94. A. Triolo, A. Mandanici, O. Russina, V. Rodriguez-Mora, M. Cutroni, C. Hardacre, M. Nieuwenhuyzen, H.-J. Bleif, L. Keller and M. A. Ramos, *J. Phys. Chem. B*, 2006, **110**, 21357-21364.
95. T. Burankova, R. Hempelmann, A. Wildes and J. P. Embs, *J. Phys. Chem. B*, 2014, **118**, 14452-14460.
96. J. P. Embs, T. Burankova, E. Reichert and R. Hempelmann, *J. Phys. Chem. B*, 2012, **116**, 13265-13271.
97. T. Burankova, G. Simeoni, R. Hempelmann, J. F. Mora Cardozo and J. P. Embs, *J. Phys. Chem. B*, 2017, **121**, 240-249.
98. T. Burankova, E. Reichert, V. Fossog, R. Hempelmann and J. P. Embs, *J. Mol. Liq.*, 2014, **192**, 199-207.
99. T. Burankova, R. Hempelmann, V. Fossog, J. Ollivier, T. Seydel and J. P. Embs, *J. Phys. Chem. B*, 2015, **119**, 10643-10651.
100. E. Mamontov, H. Luo and S. Dai, *J. Phys. Chem. B*, 2008, **113**, 159-169.
101. M. Kofu, M. Tyagi, Y. Inamura, K. Miyazaki and O. Yamamuro, *J. Chem. Phys.*, 2015, **143**, 234502/234501-234502/234510.
102. J. P. Embs, T. Burankova, E. Reichert, V. Fossog and R. Hempelmann, *Journal of the Physical Society of Japan*, 2013, **82**, SA003.
103. P. Judeinstein, S. Huet and P. Lesot, *RSC Advances*, 2013, **3**, 16604-16611.
104. C. Herriot, S. Khatun, E. T. Fox, P. Judeinstein, M. Armand, W. A. Henderson and S. Greenbaum, *The Journal of Physical Chemistry Letters*, 2012, **3**, 441-444.
105. L. S. Garca-Coln, L. F. del Castillo and P. Goldstein, *Physical Review B*, 1989, **40**, 7040-7044.
106. K. Hayamizu, S. Tsuzuki, S. Seki and Y. Umebayashi, *The Journal of Physical Chemistry B*, 2012, **116**, 11284-11291.
107. The Nobel Prize in Physics 1994, https://www.nobelprize.org/prizes/physics/1994/summary).
108. G. Kostorz and S. W. Lovesey, in *Treatise on Materials Science & Technology*, ed. G. Kostorz, Elsevier, 1979, vol. 15, pp. 1-67.
109. D. L. Price and K. Skold, in *Methods in Experimental Physics*, eds. K. Sköld and D. L. Price, Academic Press, 1986, vol. 23, pp. 1-97.
110. P. A. Egelstaff, *Thermal neutron scattering*, Academic Press, London and New York, 1965.
111. S. W. Lovesey, *Theory of neutron scattering from condensed matter*, Clarendon Press, United Kingdom, 1984.
112. G. L. Squires, *Introduction to the Theory of Thermal Neutron Scattering*, Cambridge University Press, Cambridge, 3 edn., 2012.
113. B. T. M. Willis, *Chemical Applications of Thermal Neutron Scattering*, Oxford University Press, Oxford, 1973.
114. G. Kostorz, *Volume 15 Neutron scattering*, Academic Press, United States, 1979.
115. L. de Broglie, University of Paris, 1924.

116. D. L. Price and F. Fernandez-Alonso, in *Experimental Methods in the Physical Sciences*, eds. F. Fernandez-Alonso and D. L. Price, Academic Press, 2013, vol. 44, pp. 1-136.
117. M. Bée, *Chemical Physics*, 2003, **292**, 121-141.
118. T. Graham, *Philosophical Transactions of the Royal Society of London*, 1850, **140**, 1-46.
119. T. Graham, *Philosophical Transactions of the Royal Society of London*, 1851, **141**, 483-494.
120. J. Wisniak, *Educación Química*, 2013, **24**, 506-515.
121. T. Graham, *Philosophical Transactions of the Royal Society of London*, 1861, **151**, 183-224.
122. A. Fick, *Annalen der Physik*, 1855, **170**, 59-86.
123. H. JOBIC, Dordrecht, 2006.
124. H. Jobic, in *Membrane Science and Technology*, ed. N. K. Kanellopoulos, Elsevier, 2000, vol. 6, pp. 109-137.
125. C. T. Chudley and R. J. Elliott, *Proceedings of the Physical Society*, 1961, **77**, 353.
126. H. Jobic, *Phys. Chem. Chem. Phys.*, 1999, **1**, 525-530.
127. K. S. Singwi and A. Sjölander, *Physical Review*, 1960, **119**, 863-871.
128. P. L. Hall and D. K. Ross, *Molecular Physics*, 1981, **42**, 673-682.
129. J. Dawidowski, J. R. Granada, J. R. Santisteban, F. Cantargi and L. A. R. Palomino, in *Experimental Methods in the Physical Sciences*, eds. F. Fernandez-Alonso and D. L. Price, Academic Press, 2013, vol. 44, pp. 471-528.
130. A. Meyer, R. M. Dimeo, P. M. Gehring and D. A. Neumann, *Review of Scientific Instruments*, 2003, **74**, 2759-2777.
131. E. Mamontov and K. W. Herwig, *Review of Scientific Instruments*, 2011, **82**, 085109.
132. F. Dyson, *Nature*, 2004, **427**, 297.
133. K. R. Popper, *Conjectures and refutations : the growth of scientific knowledge*, New York : Harper & Row, 1968, c1965., 1968.
134. D. Sivia and J. Skilling, *Data Analysis: A Bayesian Tutorial*, Oxford University Press, USA, 2006.
135. D. S. Sivia, C. J. Carlile, W. S. Howells and S. König, *Physica B: Condensed Matter*, 1992, **182**, 341-348.
136. F. S. Acton, *Numerical Methods that (Usually) Work*, The Mathematical Association of America, 1990.
137. L. C. Pardo, M. Rovira-Esteva, S. Busch, J. F. Moulin and J. L. Tamarit, *Physical Review E*, 2011, **84**, 046711.
138. O. Arnold, J. C. Bilheux, J. M. Borreguero, A. Buts, S. I. Campbell, L. Chapon, M. Doucet, N. Draper, R. Ferraz Leal, M. A. Gigg, V. E. Lynch, A. Markvardsen, D. J. Mikkelson, R. L. Mikkelson, R. Miller, K. Palmen, P. Parker, G. Passos, T. G. Perring, P. F. Peterson, S. Ren, M. A. Reuter, A. T. Savici, J. W. Taylor, R. J. Taylor, R. Tolchenov, W. Zhou and J. Zikovsky, *Nuclear Instruments and Methods in Physics Research Section A: Accelerators, Spectrometers, Detectors and Associated Equipment*, 2014, **764**, 156-166.
139. D. Monserrat, A. Vispa, L. C. Pardo, R. Tolchenov, S. Mukhopadhyay and F. Fernandez-Alonso, *Journal of Physics: Conference Series*, 2015, **663**, 012009.
140. L. C. Pardo, M. Rovira-Esteva, S. Busch, M. D. Ruiz-Martin and J. L. Tamarit, *Journal of Physics: Conference Series*, 2011, **325**, 012006.
141. D. S. Sivia and C. J. Carlile, *The Journal of Chemical Physics*, 1992, **96**, 170-178.
142. R. Zorn, *Nuclear Instruments and Methods in Physics Research Section A: Accelerators, Spectrometers, Detectors and Associated Equipment*, 2009, **603**, 439-445.
143. B. Frick and L. J. Fetters, *Macromolecules*, 1994, **27**, 974-980.
144. W. A. Henderson, P. Fylstra, H. C. De Long, P. C. Trulove and S. Parsons, *Phys. Chem. Chem. Phys.*, 2012, **14**, 16041-16046.

145. J. P. Belieres and C. A. Angell, *J. Phys. Chem. B*, 2007, **111**, 4926-4937.
146. A. Chahid, A. Alegria and J. Colmenero, *Macromolecules*, 1994, **27**, 3282-3288.
147. Y. Inamura, O. Yamamuro, S. Hayashi and H.-o. Hamaguchi, *Physica B: Condensed Matter*, 2006, **385-386**, 732-734.
148. F. Ferdeghini, Q. Berrod, J. M. Zanotti, P. Judeinstein, V. G. Sakai, O. Czakkel, P. Fouquet and D. Constantin, *Nanoscale*, 2017, **9**, 1901-1908.
149. A. Abe, R. L. Jernigan and P. J. Flory, *Journal of the American Chemical Society*, 1966, **88**, 631-639.
150. M. E. V. Valkenburg, R. L. Vaughn, M. Williams and J. S. Wilkes, *Thermochimica Acta*, 2005, **425**, 181-188.
151. T. Murphy, L. M. Varela, G. B. Webber, G. G. Warr and R. Atkin, *The Journal of Physical Chemistry B*, 2014, **118**, 12017-12024.
152. B. Aoun, M. A. Gonzalez, J. Ollivier, M. Russina, Z. Izaola, D. L. Price and M.-L. Saboungi, *J. Phys. Chem. Lett.*, 2010, **1**, 2503-2507.
153. R. Lefort, D. Morineau, R. Guégan, C. Ecolivet, M. Guendouz, J.-M. Zanotti and B. Frick, *Phys. Chem. Chem. Phys.*, 2008, **10**, 2993-2999.
154. V. K. Sharma, S. Mitra, G. Verma, P. A. Hassan, V. Garcia Sakai and R. Mukhopadhyay, *The Journal of Physical Chemistry B*, 2010, **114**, 17049-17056.
155. J. M. Borreguero and V. E. Lynch, *Journal of Chemical Theory and Computation*, 2016, **12**, 9-17.

Chapter 7: Appendix

7.1 d_3-EAN data from HFBS

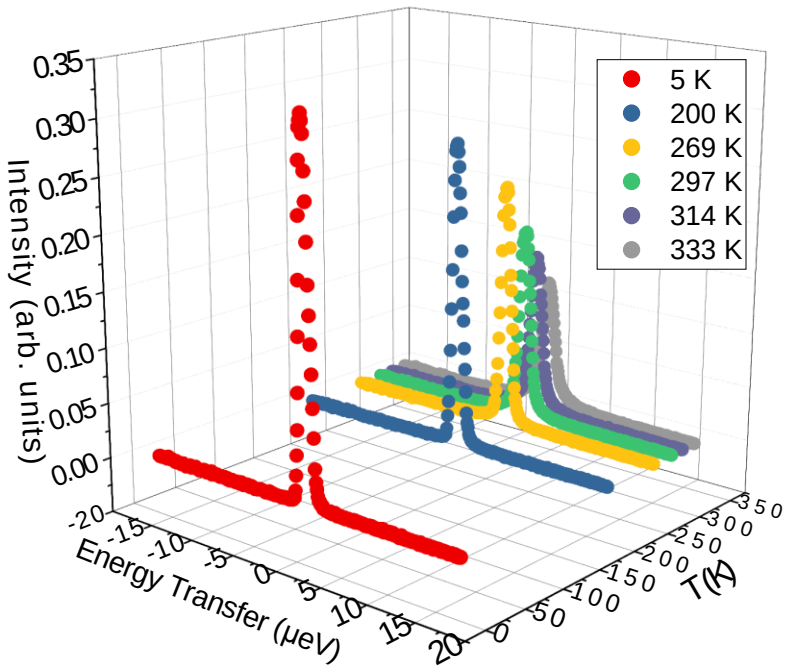

Figure A1. Raw unfitted Dynamic Structure Factor S(Q) of d_3-EAN at Q = 0.3085 Å^{-1}.

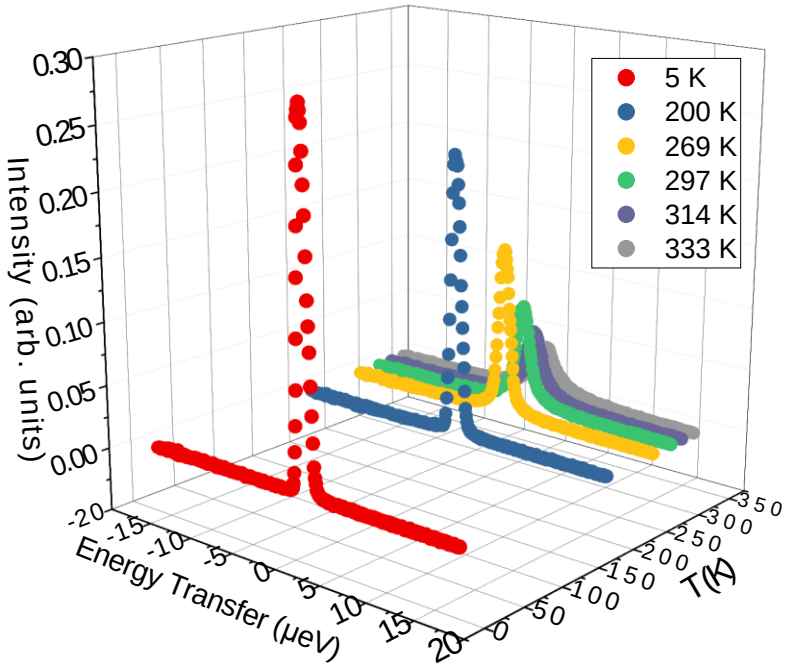

Figure A2. Raw unfitted Dynamic Structure Factor S(Q) of d_3-EAN at Q = 0.5134 Å^{-1}.

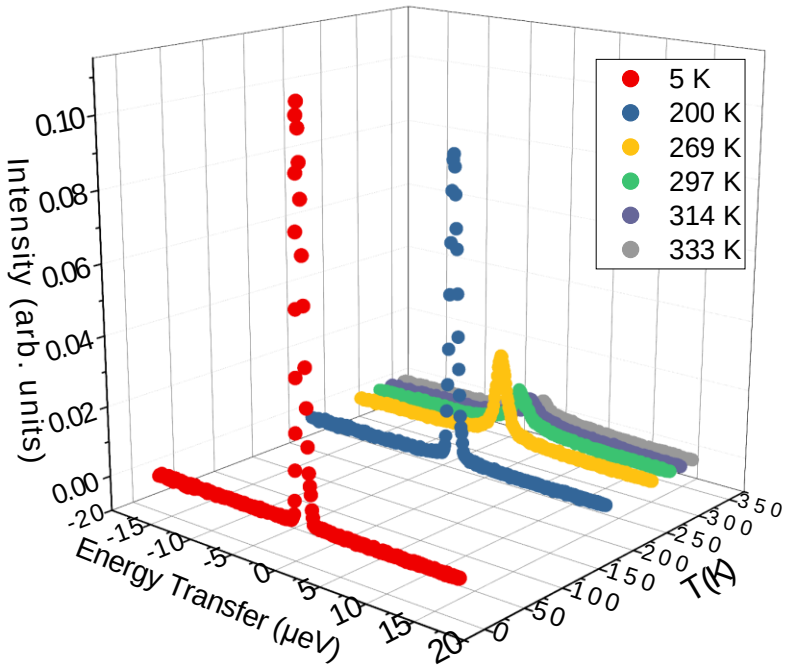

Figure A3. Raw unfitted Dynamic Structure Factor S(Q) of d_3-EAN at Q = 0.6830 Å^{-1}.

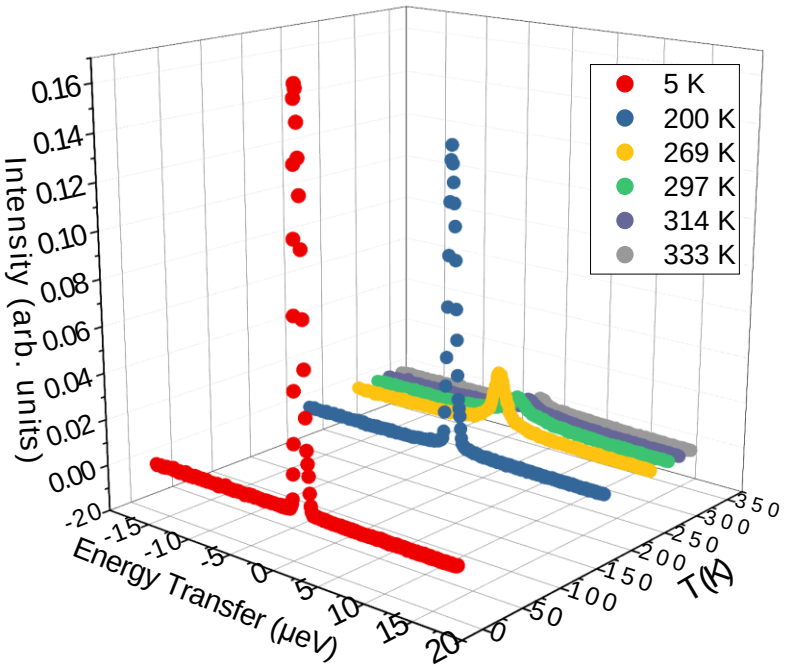

Figure A4. Raw unfitted Dynamic Structure Factor S(Q) of d_3-EAN at Q = 0.9307 Å^{-1}.

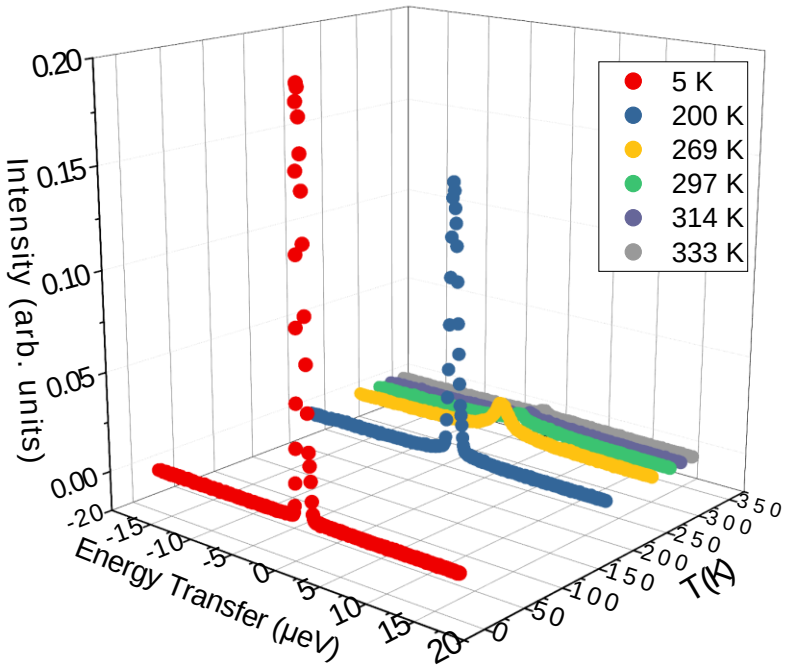

Figure A5. Raw unfitted Dynamic Structure Factor S(Q) of d_3-EAN at Q = 1.1614 Å^{-1}.

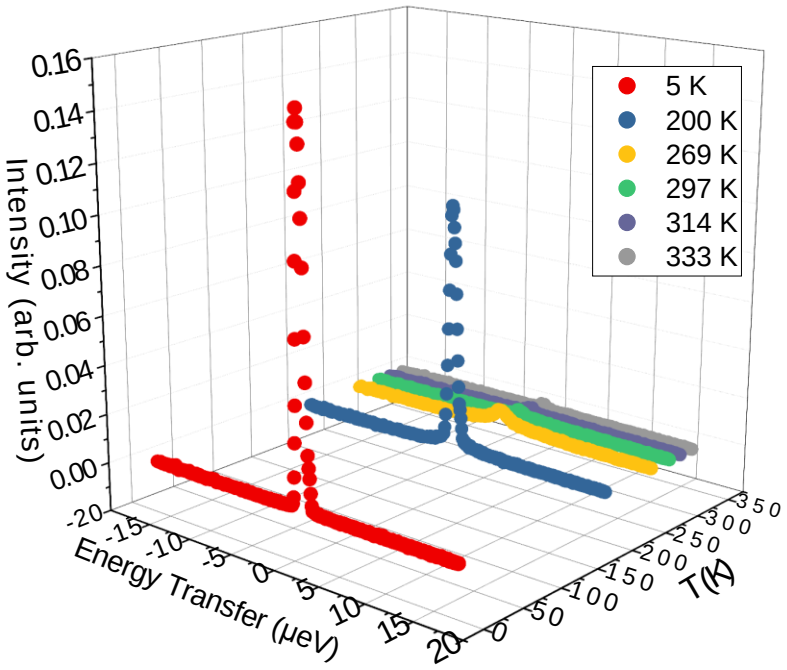

Figure A6. Raw unfitted Dynamic Structure Factor S(Q) of d_3-EAN at Q = 1.3709 Å^{-1}.

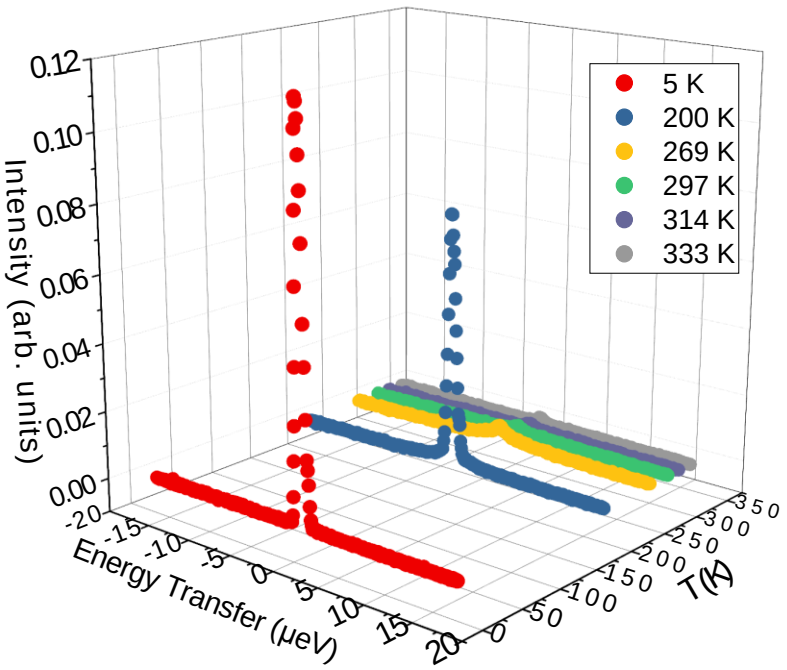

Figure A7. Raw unfitted Dynamic Structure Factor S(Q) of d_3-EAN at Q = 1.5553 Å^{-1}.

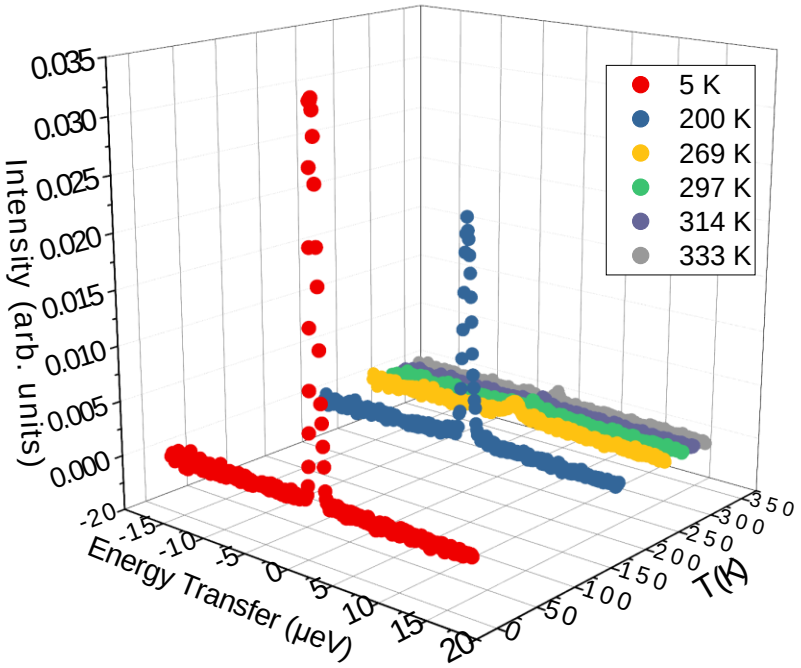

Figure A8. Raw unfitted Dynamic Structure Factor S(Q) of d_3-EAN at Q = 1.7124 Å^{-1}.

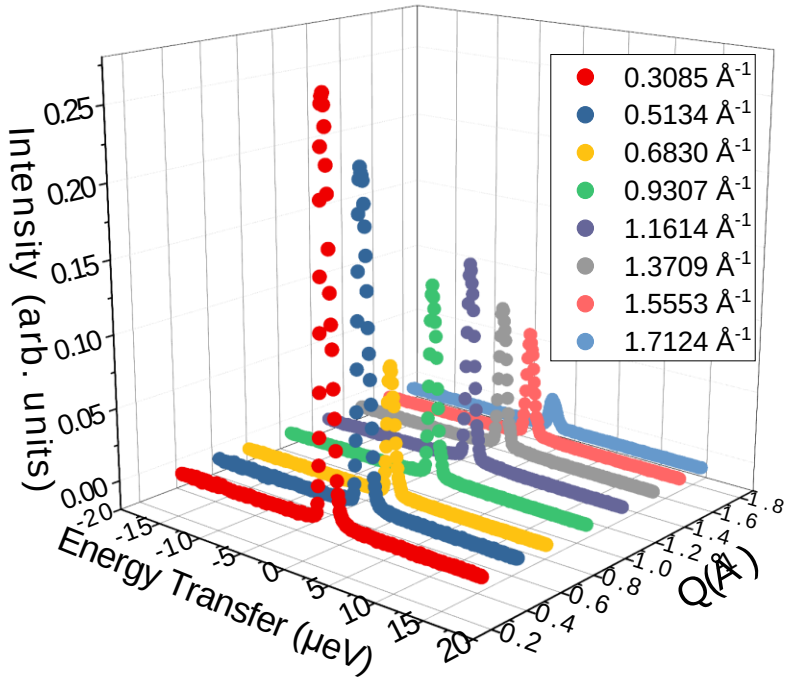

Figure A9. Raw unfitted Dynamic Structure Factor S(Q) of d_3-EAN at T = 200 K.

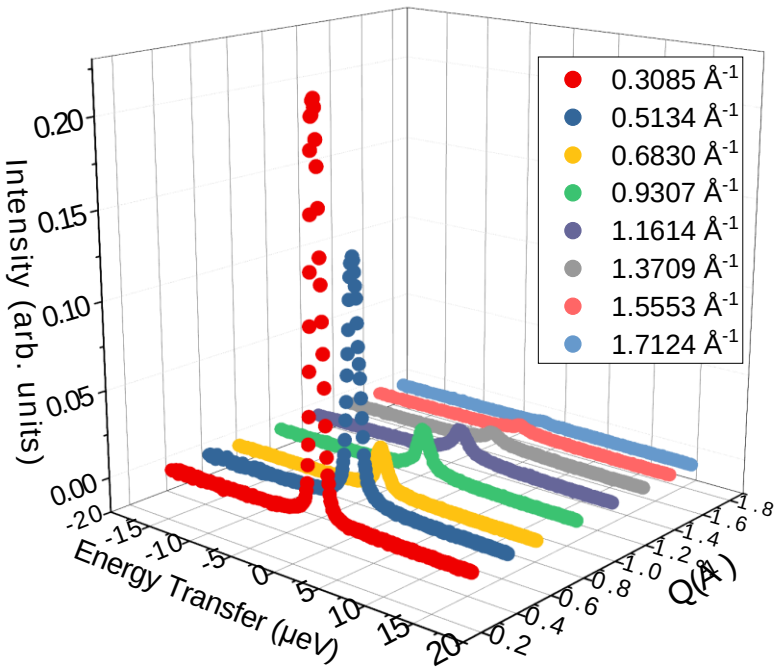

Figure A10. Raw unfitted Dynamic Structure Factor S(*Q*) of d_3-EAN at *T* = 269 K.

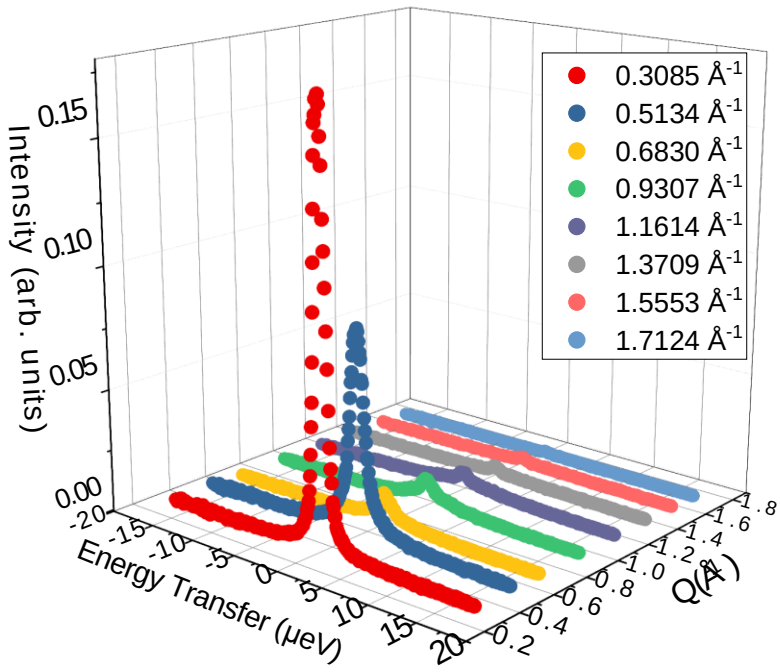

Figure A11. Raw unfitted Dynamic Structure Factor S(*Q*) of d_3-EAN at *T* = 297 K.

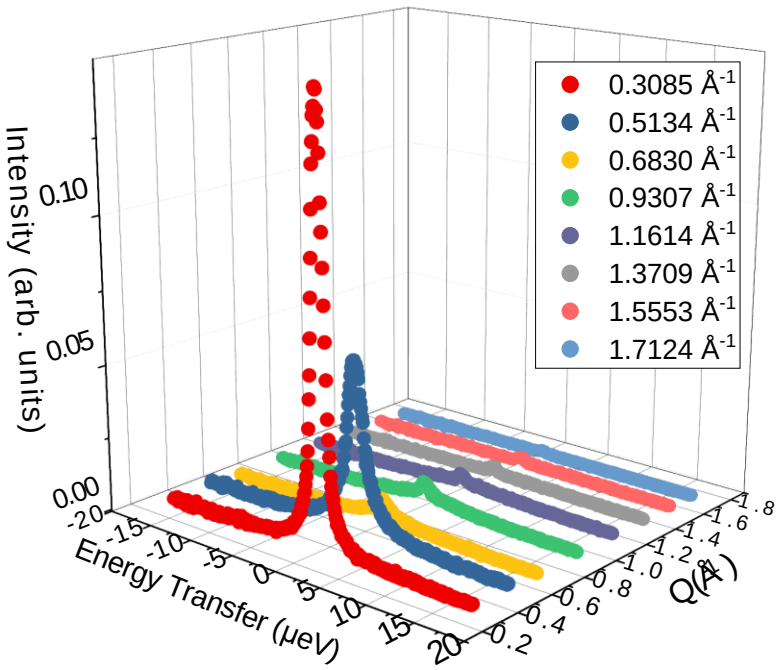

Figure A12. Raw unfitted Dynamic Structure Factor S(Q) of d_3-EAN at T = 314 K.

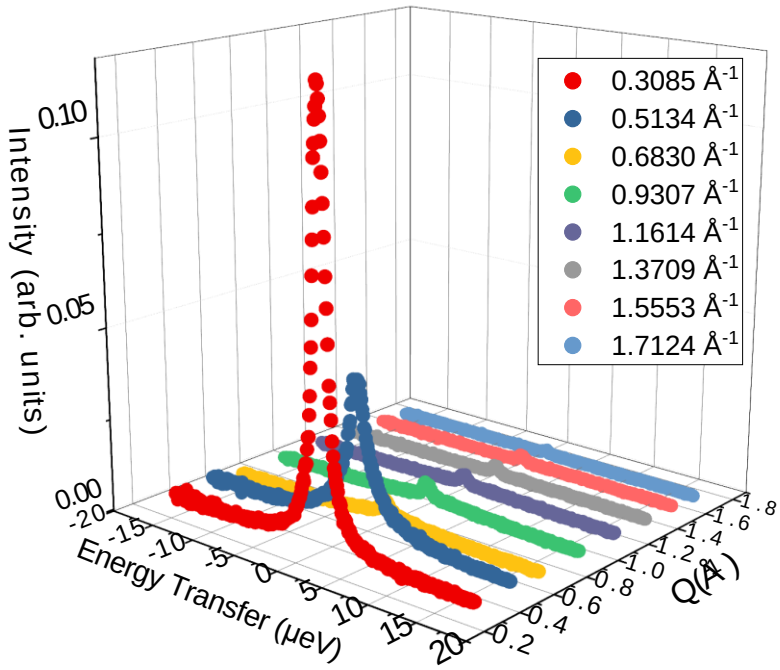

Figure A13. Raw unfitted Dynamic Structure Factor S(Q) of d_3-EAN at T = 333 K.

7.2 EAN data from BASIS

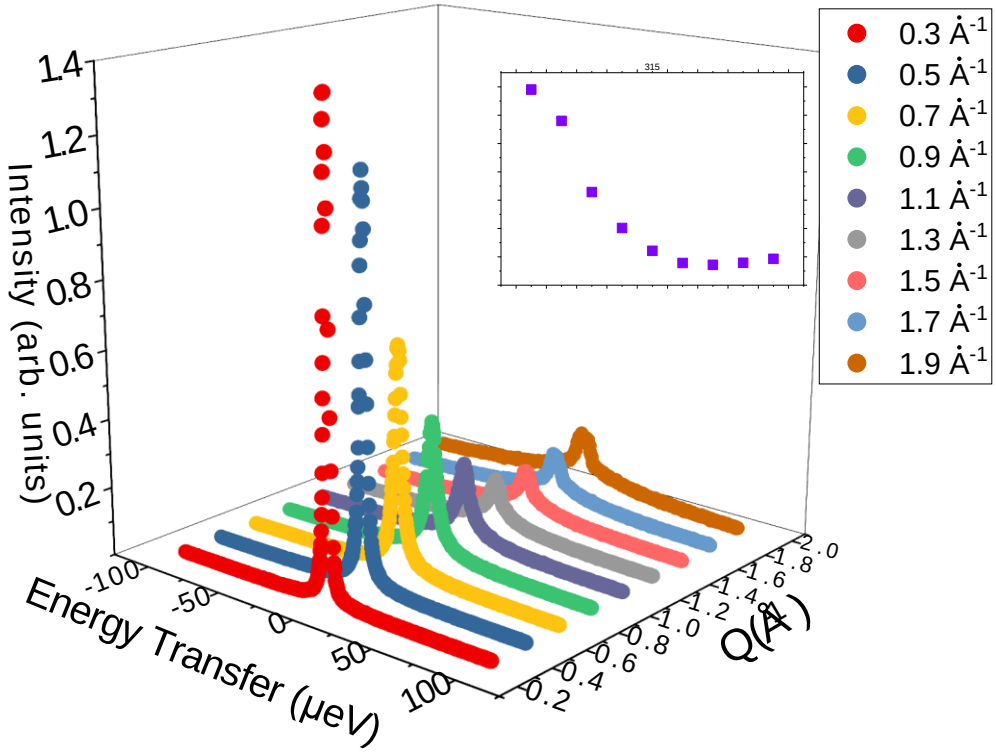

Figure A14. Raw unfitted Dynamic Structure Factor S(*Q*) of *H*-EAN at *T* = 315 K. Inset shows the relative peak intensities.

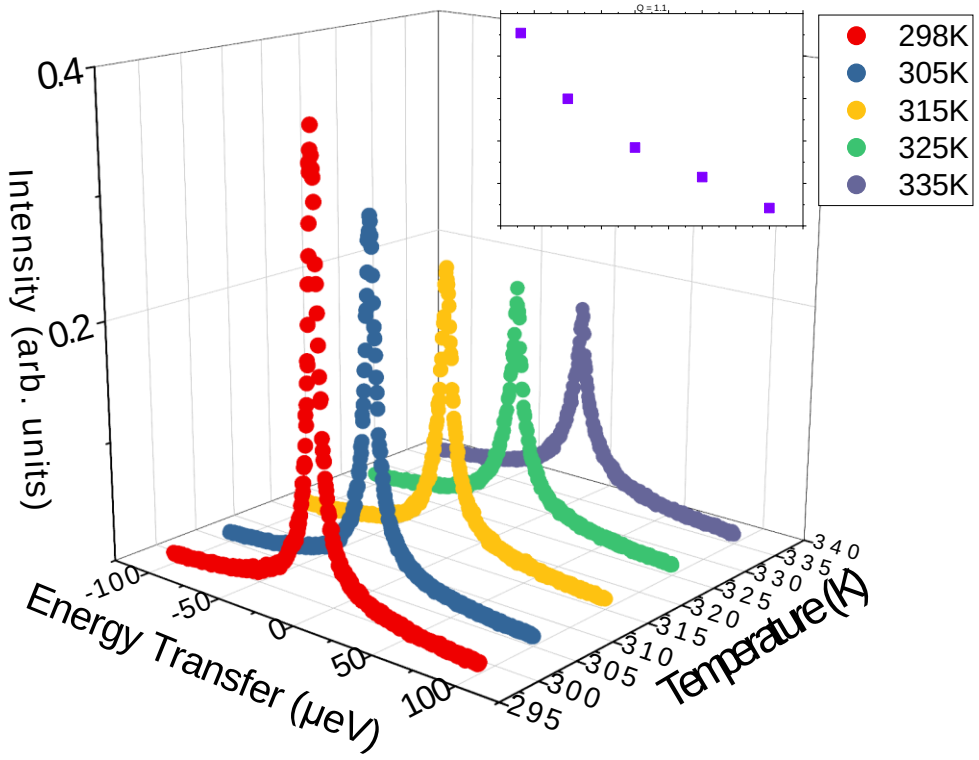

Figure A15. Raw unfitted Dynamic Structure Factor S(*Q*) of *H*-EAN at *Q* = 1.1 Å^{-1}.There is temperature dependence of intensity and line broadness, typical of QENS structure factors. Inset shows the relative peak intensities.

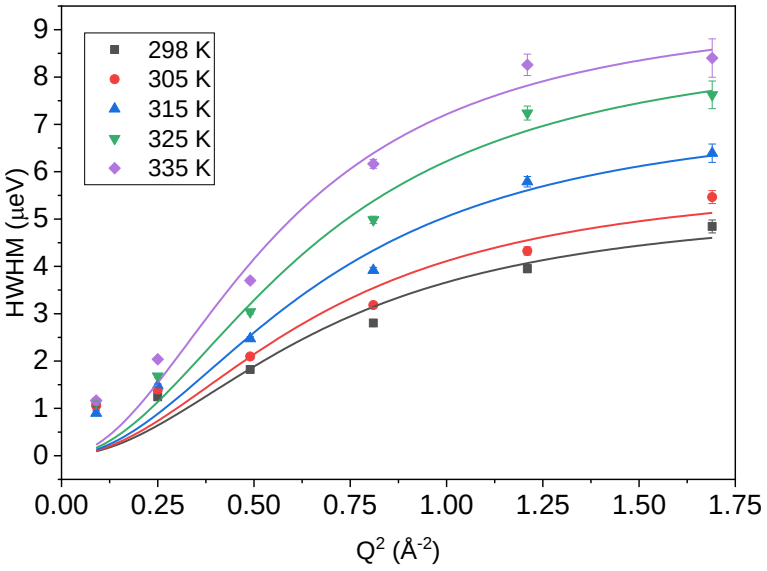

Figure A16. Fit results of the temperature dependence for the narrow Lorentzian component in BASIS data. Half-width half maximum $\Gamma_{1/2}$ as a function of Q^2 at liquid phase temperatures (> 285 K) is shown. Solid lines were fitted with the Singwi-Sjölander jump diffusion model.

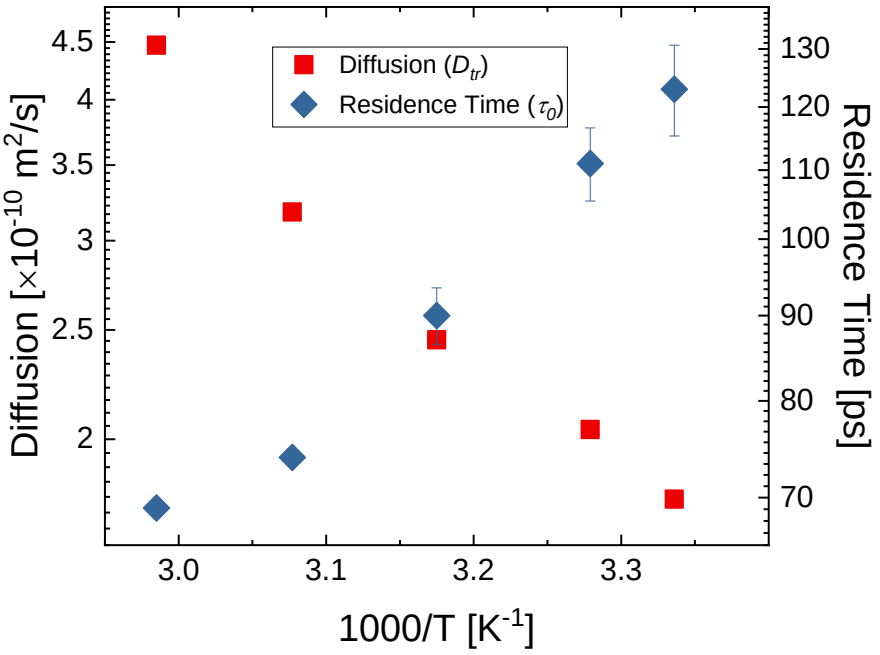

Figure A17. Arrhenius Plot of the diffusion coefficient *D* (red symbols) describing long-range diffusion as a function of the inverse temperature. Symbols denote the values of *D* obtained for the five liquid phase temperatures (298, 305, 315, 325, and 335K respectively. Residence time τ_0 (blue symbols) as a function of the inverse temperature is also shown; Note as temperature increases, residence time is decreasing.

7.3 d_3-PAN Data from HFBS

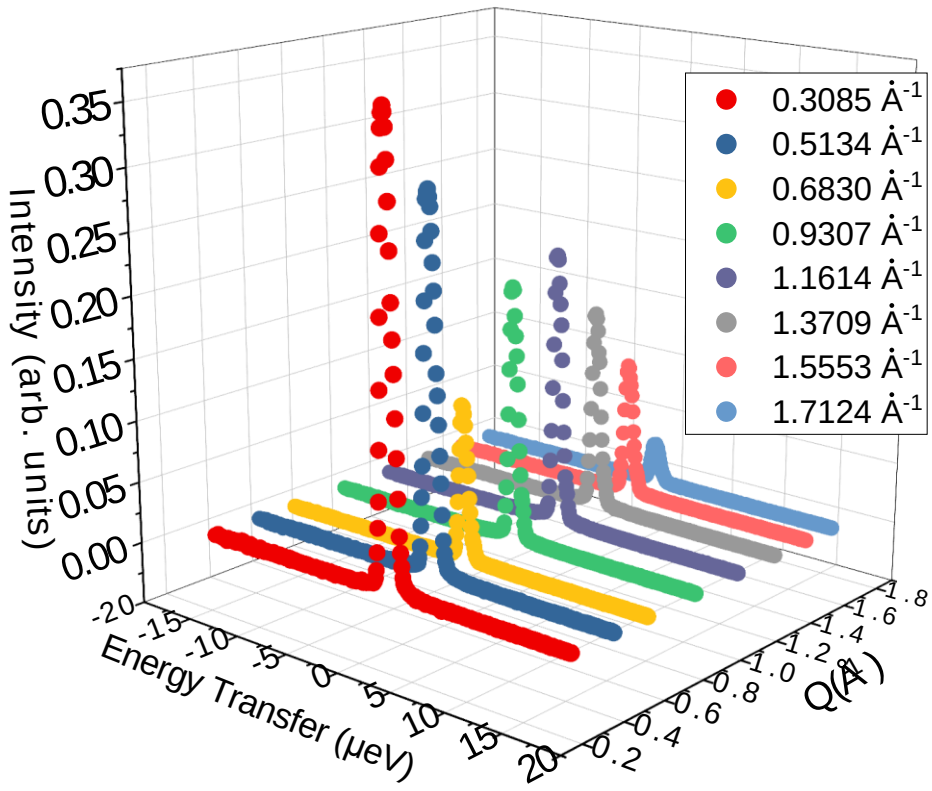

Figure A18. Raw unfitted Dynamic Structure Factor S(Q) of d_3-PAN at T = 180 K. The data is taken on the HFBS instrument from a Q range of 0.3085 Å^{-1} < Q < 1.712 Å^{-1}.

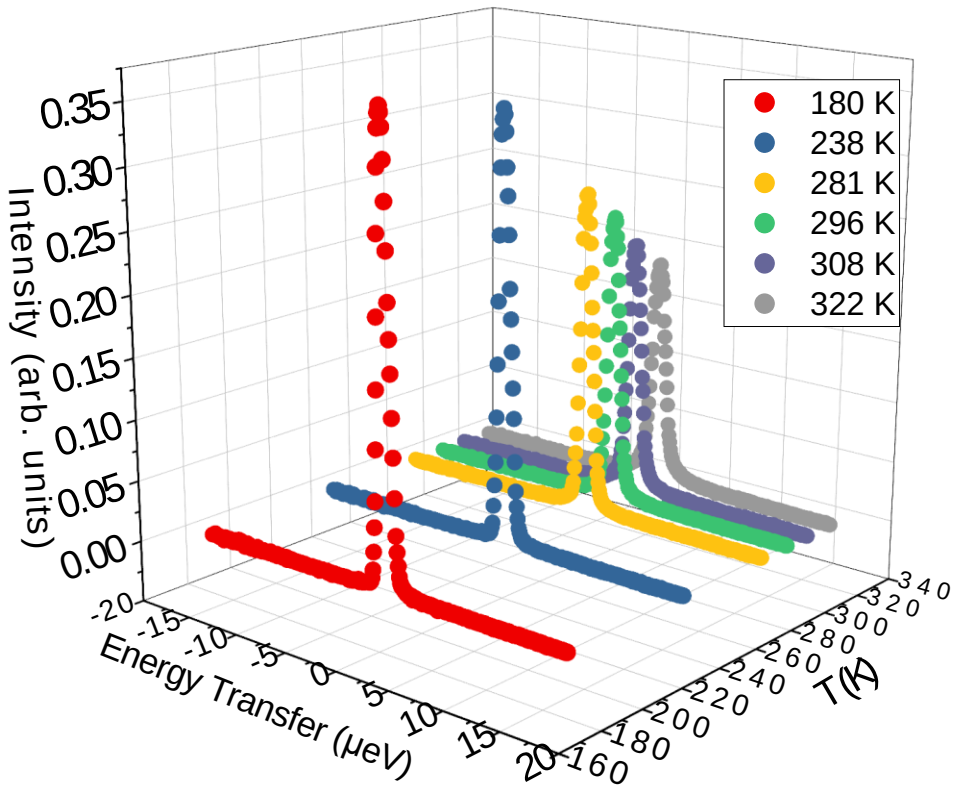

Figure A19. Raw unfitted Dynamic Structure Factor S(Q) of d_3-PAN at Q = 0.3085 Å^{-1}. There is temperature dependence of intensity and line broadness, typical of QENS structure factors.

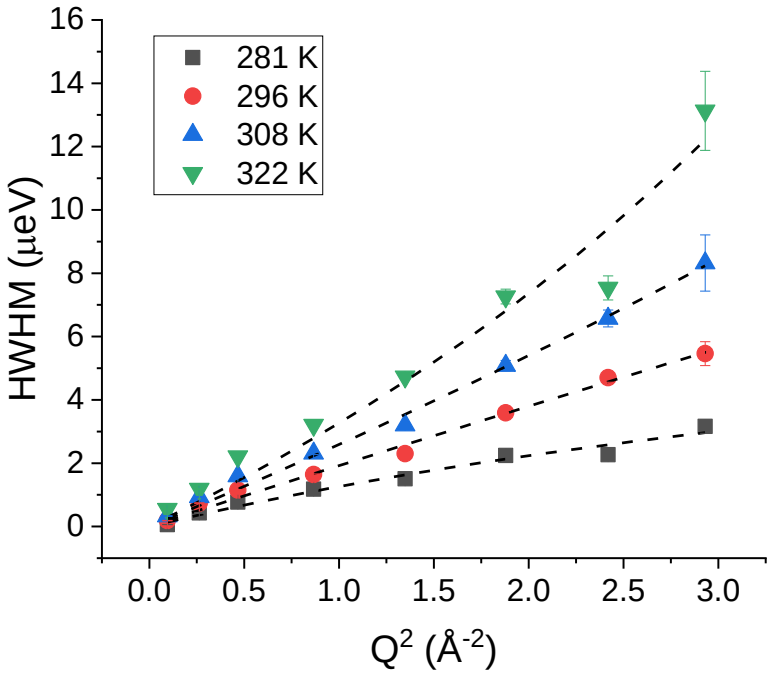

Figure A20. Fit results of the temperature dependence for the single Lorentzian component in HFBS data. Half-width half maximum $\Gamma_{1/2}$ as a function of Q^2 at liquid phase temperatures (> 281 K) is shown. Dashed lines were fitted with the Singwi-Sjölander jump diffusion model.